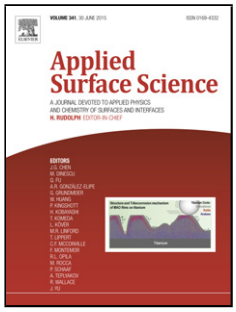

Title: Laser polishing of 3D printed mesoscale components

Authors: Debajyoti Bhaduri, Pavel Penchev, Afif Batal, Stefan Dimov, Sein Leung Soo, Stella Sten, Urban Harrysson, Zhenxue Zhang, Hanshan Dong

PII: S0169-4332(17)30234-9
DOI: http://dx.doi.org/doi:10.1016/j.apsusc.2017.01.211
Reference: APSUSC 35006

To appear in: *APSUSC*

Received date: 13-7-2016
Revised date: 2-12-2016
Accepted date: 21-1-2017

Please cite this article as: Debajyoti Bhaduri, Pavel Penchev, Afif Batal, Stefan Dimov, Sein Leung Soo, Stella Sten, Urban Harrysson, Zhenxue Zhang, Hanshan Dong, Laser polishing of 3D printed mesoscale components, Applied Surface Science http://dx.doi.org/10.1016/j.apsusc.2017.01.211

Laser polishing of 3D printed mesoscale components

Debajyoti Bhaduri[1,*], Pavel Penchev[1], Afif Batal[1], Stefan Dimov[1], Sein Leung Soo[1], Stella Sten[2], Urban Harrysson[2], Zhenxue Zhang[3], Hanshan Dong[3]

[1]Department of Mechanical Engineering, School of Engineering, University of Birmingham, Edgbaston, Birmingham, B15 2TT, UK

[2]Digital Metal, Höganäs AB, 263 83 Höganäs, Sweden

[3]School of Metallurgy and Materials, University of Birmingham, Edgbaston, Birmingham, B15 2TT, UK

* Corresponding author

Emails: debajyoti.bhaduri@gmail.com, d.bhaduri@bham.ac.uk

Graphical abstract

Laser polishing of various engineered materials such as glass, silica, steel, nickel and titanium alloys, has attracted considerable interest in the last 20 years due to its superior flexibility, operating speed and capability for localised surface treatment compared to conventional mechanical based methods. The paper initially reports results from process optimisation experiments aimed at investigating the influence of laser fluence and pulse overlap parameters on resulting workpiece surface roughness following laser polishing of planar 3D printed stainless steel (SS316L) specimens. A maximum reduction in roughness of over 94% (from ~3.8 to ~0.2 µm S_a) was achieved at the optimised settings (fluence of 9 J/cm^2 and overlap factors of 95% and 88-91% along beam scanning and step-over directions respectively), shown in Fig. A1. Subsequent analysis using both X-ray photoelectron spectroscopy (XPS) and glow discharge optical emission spectroscopy (GDOES) confirmed the presence of surface oxide layers (predominantly consisting of Fe and Cr phases) up to a depth of ~0.5 µm when laser polishing was performed under normal atmospheric conditions. Conversely, formation of oxide layers was negligible when operating in an inert argon gas environment. The microhardness of the polished specimens was primarily influenced by the input thermal energy, with greater sub-surface hardness (up to ~50-60%) recorded in the samples processed with higher energy density. Additionally, all of the polished surfaces were free of the scratch marks, pits, holes, lumps and irregularities that were prevalent on the as-received stainless steel samples. The optimised laser polishing technology was consequently implemented for serial finishing of structured 3D printed mesoscale SS316L components. This led to substantial reductions in areal S_a and S_t parameters by 75% (0.489 to 0.126 µm) and 90% (17.71 to 1.21 µm) respectively, without compromising the geometrical accuracy of the native 3D printed samples, see Fig. A2.

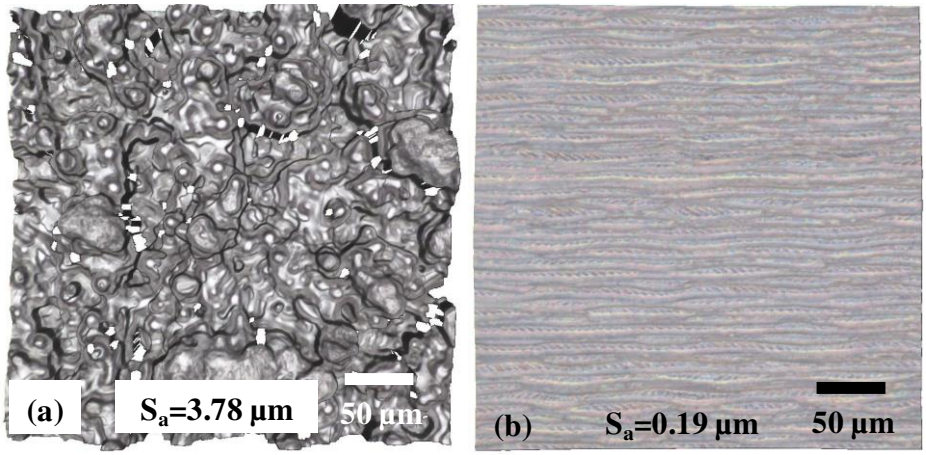

Fig. A1 Areal surface topographies of: (a) parent material; (b) laser polished areas processed with fluence: 9 J/cm^2, pulse overlap along X: 95%, pulse overlap along Y: 88%.

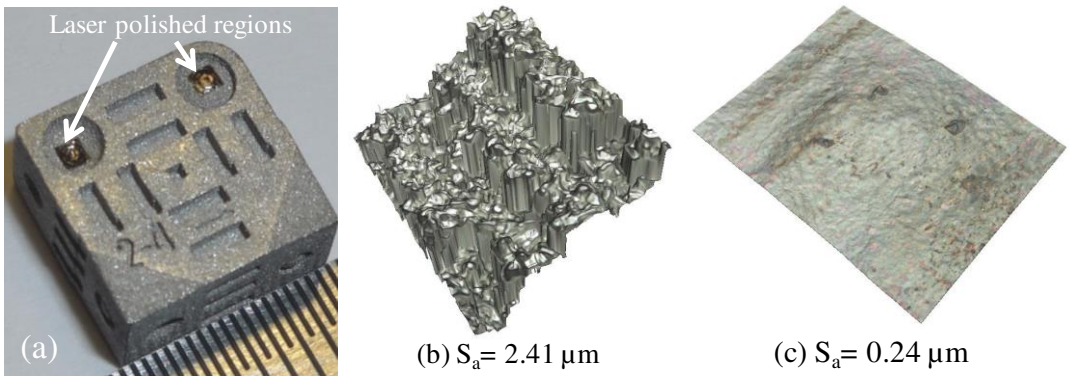

Fig. A2 (a) Laser polished regions on Digital Metal structured SS316L parts; (b) as-received surface; (c) laser polished surface (area: 287×218 µm).

Highlights

- Process optimisation for laser polishing novel 3D printed SS316L parts
- Evaluating the effects of key polishing parameters on SS316L surface roughness
- Detailed spectroscopic analysis of oxide layer formation due to laser polishing
- Comparative surface integrity analysis of SS parts polished in air and argon
- A maximum reduction in roughness of over 94% achieved at optimised polishing settings

Abstract

Laser polishing of various engineered materials such as glass, silica, steel, nickel and titanium alloys, has attracted considerable interest in the last 20 years due to its superior flexibility, operating speed and capability for localised surface treatment compared to conventional mechanical based methods. The paper initially reports results from process optimisation experiments aimed at investigating the influence of laser fluence and pulse overlap parameters on resulting workpiece surface roughness following laser polishing of planar 3D printed stainless steel (SS316L) specimens. A maximum reduction in roughness of over 94% (from ~3.8 to ~0.2 µm S_a) was achieved at the optimised settings (fluence of 9 J/cm^2 and overlap factors of 95% and 88-91% along beam scanning and step-over directions respectively). Subsequent analysis using both X-ray photoelectron spectroscopy (XPS) and glow discharge optical emission spectroscopy (GDOES) confirmed the presence of surface oxide layers (predominantly consisting of Fe and Cr phases) up to a depth of ~0.5 µm when laser polishing was performed under normal atmospheric conditions. Conversely, formation of oxide layers was negligible when operating in an inert argon gas environment. The microhardness of the polished specimens was primarily influenced by the input thermal energy, with greater sub-surface hardness (up to ~50-60%) recorded in the samples processed with higher energy density. Additionally, all of the polished surfaces were free of the scratch marks, pits, holes, lumps and irregularities that were prevalent on the as-received stainless steel samples. The optimised laser polishing technology was consequently implemented for serial finishing of structured 3D printed mesoscale SS316L components. This led to substantial reductions in areal S_a and S_t parameters by 75% (0.489 to 0.126 µm) and 90% (17.71 to 1.21 µm) respectively, without compromising the geometrical accuracy of the native 3D printed samples.

Keywords

Laser polishing; fluence; pulse distance; 3D printing; stainless steel; surface integrity

1. Introduction

Additive manufacturing (AM) or 3D printing is rapidly developing as a viable technology for producing complex components as it offers many advantages over conventional processing. This includes greater design freedom as well as the capability to efficiently produce complex parts with intricate internal and external structures. While there is evidence of growing interest and initial utilisation of AM processes in several industries such as the automotive, aerospace, opto-electronic and biomedical sectors [1], uptake of this technology on a larger production scale remains limited. This is primarily due to shortcomings of current AM processes relating to achievable workpiece geometrical accuracy and surface integrity, with parts generally suffering from poor surface roughness (typically ranging from ~5 to 15 µm R_a), stair-step effects on surfaces, balling, adverse residual stresses and low dimensional precision [2]. Therefore, post-process operations such as sand blasting, machining, etching, electro-polishing or plasma spraying is often employed for AM components to meet functional tolerances and surface integrity requirements. Some of these methods however are time consuming and not viable particularly for products with complex geometries. A potential alternative is laser polishing (LP), which is a flexible, contactless method that can be fully automated without the need for dedicated equipment. The technology has been continuously developed over the past two decades and successfully employed for improving the surface morphologies of components made from various materials such as diamond, glass, silica and metals including steel, nickel/titanium alloys and to a somewhat lesser extent, aluminium alloys [3]. The present paper details results from experimental trials to

evaluate the performance of laser polishing for finishing additively manufactured stainless steel surfaces. The effects of varying laser fluence and pulse overlap factors on workpiece surface roughness were assessed, followed by an analysis of oxide layer formation, microstructure and microhardness after polishing at different fluence levels under atmospheric and argon environments.

2. Literature review and research motivation

2.1. Review of laser polishing research

Polishing using laser irradiation can be achieved through three different process mechanisms, which are large area ablation, localised ablation and re-melting at macro (over depths of 20-200 µm) or micro (over depths of 0.5-5 µm) polishing regimes [4]. The majority of research on LP however has focussed primarily on the re-melting mechanism due to several advantages compared to the ablation based methods, such as greater scope for automated operation, shorter machining times, reduced environmental impact and better user control of surface roughness and localised processing capability [4].

Re-melting is initiated when material from surface asperities is redistributed into adjacent troughs/valleys to form a molten pool due to surface tension as a laser beam passes over the workpiece. This leads to a decrease in peak-to-valley heights of the initial surface asperities [3]. A schematic illustrating the re-melting mechanism in LP is given in Fig. 1(a) while its effect on surface topography is shown in Fig. 1(b).

2.1.1. Laser polishing of non-metallic materials

Surface treatment of thick (>100 µm) and thin (<100 µm) diamond films (deposited by chemical vapour deposition) using LP was introduced in the mid-1990s, with the process demonstrating remarkable reduction in polishing times compared to mechanical methods [5,

6]. It was reported that mechanical polishing techniques typically required 12 to 28 hours in order to achieve optical quality surface finish for 150-400 µm thick diamond films over an area of 8×10 mm^2, while LP processing time was less than 1 hour for a 5×5 mm^2 area [6]. However, the average surface roughness (R_a) following LP was of the order of micrometres whereas the mechanical based treatment was capable of producing roughnesses in the nanometre range. Thus, LP is usually recommended as an initial "rough" polishing operation in order to reduce the overall processing time for generating optical quality surfaces.

Apart from thick/thin diamond films, LP has also been employed for the finishing of fused silica/glass parts [7-11]. Bol'shepaev and Katomin [7] reported that workpiece surface cracking following LP of fused silica was due to thermal stresses induced by the laser beam and consequently recommended pre-heating the workpiece to near annealing temperatures (500-600°C) prior to polishing. In order to achieve an acceptable surface finish Wang et al. [8] showed that an optimum range of laser energy density (800 to 1100 J/cm^2) was required for LP of silica, below which no obvious surface modifications occurred whilst higher energy densities led to vaporisation and breakdown of SiO_2 to SiO. However, in another study by Hildebrand et al. [10], it was observed that the final surface roughness was largely influenced by the initial roughness and waviness of the as-received workpieces. Heidrich et al. [11] proposed a three-step manufacturing route for producing optical components, starting with high speed laser ablation followed by LP and finally high precision laser ablation. Spherical, aspherical and freeform surfaces were successfully laser polished with comparable roughness and waviness to those achieved on planar surfaces.

2.1.2. Laser polishing of steel and cast iron

Much of the published research concerning LP of ferrous materials has predominantly involved tool steels, although several carbon and stainless steel grades have also been

investigated. Brinksmeier et al. [12] compared LP and abrasive flow machining against conventional abrasive polishing for producing X40Cr13 stainless steel moulds. Despite roughness of the laser polished structures being within 400 to 600 nm R_a, the surfaces were still found to be short of optical quality standards. Avilés et al. [13, 14] assessed the surface integrity and fatigue strength of laser polished AISI 1045 steel specimens performed under atmospheric and N_2 gas environments. A heat affected zone (HAZ) up to a depth of 100-150 µm beneath the workpiece surface was evident in both cases but with differences in the surface/subsurface characteristics. In particular, the formation of oxide layers, micro-cracks and inclusions were observed after laser polishing under normal atmospheric condition while a pearlitic to martensitic transformation together with compressive residual stresses up to 200 MPa in the HAZ was apparent when operating in a N_2 environment. Furthermore, the fatigue strength of samples processed under an inert gas condition was ~7.5% higher than those polished in air [14]. The performance of diode-pumped solid-state and CO_2 lasers in continuous (CW) mode for LP of DIN 1.2379 (AISI D2) tool steel was evaluated by Ukar et al. [15], who also developed a mathematical model to predict the resulting surface roughness [16]. While both laser sources achieved comparable reduction in surface roughness (75-80%), the solid-state system was found to be more efficient due to its larger beam spot diameter of 2 mm compared to 1.04 mm for the CO_2 laser.

The effects of process parameters such as energy density [17-19], scanning speed [20] and step-over distance [21] on the quality of laser polished surfaces have been studied by numerous researchers, with the majority concluding that laser energy density has the strongest influence on resulting surface integrity [19]. Laser energy density is typically controlled by varying the focal offset distance (FOD) from the workpiece, which correspondingly alters the diameter of the beam. Chow et al. [17] investigated laser micropolishing (LµP) of AISI H13 steel surfaces at FOD's of 1.3-2.9 mm. A decrease in

surface roughness of up to 39.7% was achieved with a FOD greater than 2.2 mm. Similarly, Pfefferkorn et al. [18] showed that beam diameter was a significant factor affecting the roughness of pulsed laser polished S7 tool steel parts.

Comprehensive research has been undertaken on predicting and optimising workpiece surface roughness following pulsed laser micro polishing (PLμP) of tool [22, 23] and stainless [24] steels. Viscous damping of melt pool oscillations (capillary regime) together with Marangoni flows caused by surface tension gradients (thermo-capillary regime) were identified as the predominant smoothening mechanisms [24]. Under certain processing conditions, some of the polished specimens exhibited open surface cracks (~5 to 10 μm in length) due to variations in residual stresses within the re-solidified layers [22].

Laser polishing of cast iron has also been assessed however it was found that the free graphite elements within the material structure hindered process efficiency due to its high melting temperature (~1500 K). However, by performing the LP process in a controlled CO_2 environment, it was possible to eliminate the graphite particles from the surface and hence reduce surface roughness by 88% [25].

2.1.3. Laser polishing of nickel and titanium alloys

Perry et al. [26] studied the influence of pulse duration and scanning speed when laser polishing micro-fabricated nickel specimens. Finite element (FE) and fluid flow simulations predicted that smoother surfaces were obtained with longer pulse durations. Corresponding experimental validation trials carried out at pulse durations of 300 and 650 ns, reduced the average workpiece surface roughness R_a to 66 and 47 nm respectively, from an initial value of 95-96 nm. Hafiz et al. [27] evaluated the feasibility of using a picosecond laser for micro-polishing of Inconel 718 and in particular the effects of laser fluence/energy density. Ablation and melting regimes were prevalent when operating at fluence levels of 0.19-0.24 J/cm^2 and

0.13-0.18 J/cm^2 respectively. However a transition zone between ablation and melting was also evident that led to inconsistent formation of grooves and slots.

The application of PLµP for finishing of titanium (Ti) alloys has also been explored [28-31]. Surface cracking was typically observed when polishing Ti-6Al-4V in air due to oxidation but which can be avoided by processing in an Ar controlled environment [28]. Similar defects were also reported by Yermachenko et al. [32] when LP VT16 titanium alloy in air. A comparative study involving the LµP of Ti-6Al-4V and martensitic tool steel with an additional laser beam for pre-heating the workpiece surfaces was detailed by Nüsser et al. [33] . Although the dual beam approach was detrimental for the tool steel due to increased formation of martensite, improved surface finish (36% lower roughness) was observed for the Ti-6Al-4V material due to the extended melt duration. In another study by Kumstel and Kirsch [34], LP processing time was found to be lower for Ti-6Al-4V (7 s/cm^2) compared to Inconel 718 (10 s/cm^2) and tool steel (60 s/cm^2). Although the LP of Ti is most effective when performed in air (in terms of reduction in roughness), localised molten globules and oxidation zones are generally present on the polished surfaces. Therefore, the use of an assisted inert gas medium is crucial when processing Ti alloys and preferably delivered at optimised pressures [35].

2.1.4. Laser polishing of AM components

Remos-Grez and Bourell [36] investigated the use of non-tactile LP process for surface finishing of free-form selective laser sintered (SLS) iron-copper parts with a particular focus on assessing two melting regimes, surface shallow melting (SSM) and surface over melting (SOM), which has a significant influence on final surface integrity. The former was characterised by fast melting and re-solidification of surface asperities that produced a smoother finish, while SOM resulted in a deeper melting of a layer below the surface valleys

and a higher roughness when LP was carried out with elevated laser energy density. Another study carried out by Lamikiz et al. [37] on the LP of SLS parts (made of 60% sintered AISI 420 stainless steel and 40% infiltrated bronze) at different laser energy densities and beam scanning speeds showed that an 80% reduction in surface roughness from 7.5 to ~1.2 μm R_a was possible when operating at optimised process conditions. As for parts manufactured via selective laser melting (SLM), several publications have concluded that a LP step after each intermediate layer (20-30 μm thickness) or following deposition of the final layer can be beneficial for improving component surface integrity [2, 38-40]. This includes increased workpiece microhardness and material density/sealed the surface porosities together with microstructure refinement leading to improved micro-machinability. Marimuthu et al. [41] developed a computational fluid dynamics (CFD) based numerical model to understand the melt pool dynamics during LP with laser energy, beam scanning speed and focal offset distance as the variable parameters and its associated influence on resulting surface roughness. Input thermal energy was identified as the key process parameter affecting melt pool convection, and thereby controlling the resulting surface quality. A higher energy density resulted in increased melt pool velocity that subsequently deteriorated the final surface finish. Conversely, a low melt pool velocity aided in achieving wider polished track width, thereby improving the surface quality. Experiments utilising optimised process parameters for LP of SLM fabricated Ti-6Al-4V parts demonstrated an improvement in surface roughness from 10.2 to 2.4 μm [41]. Likewise, work on LP of laser clad SS316L specimens also revealed a substantial reduction in surface roughness of up to 96%, from 21 to 0.79 μm S_a [42].

Important LP investigations with their key process variables are listed in Table 1. They were used in defining the LP requirements in this research and also for identifying the LP processing window that was investigated.

2.2. Research motivation

As the melting temperature of metal powders is exceeded in laser/electron beam based AM processes, the fabricated parts typically suffer from adverse residual stresses and poor fatigue properties. The design of a suitable support structure is also a pre-requisite for successful SLM or electron beam melting (EBM) applications. To address some of these limitations, a novel 3D printing technology for metallic materials commercially known as Digital Metal® (DM), was developed [43]. This two stage process requires "green" parts to be initially produced in a metal powder bed by a precision layer by layer ink-jet printing followed by a secondary sintering step, as shown in Fig. 2. The technology is capable of producing complex SS316L parts having up to 97% density and which is independent of the printing orientation [43]. In addition, contrary to the SLS or SLM fabricated components, there is no distortion of the green parts or induced residual stress as printing is carried out at room temperature. While traditional AM techniques typically produce parts with R_a in the range of 5-7 μm, and sometimes as high as 10-30 μm [44], DM manufactured components exhibit relatively lower surface roughness, typically in the order of ~ 3 to 4 μm R_a. Despite this, micro/mesoscale components produced with DM technology still require post-process operations to obtain the necessary functional surface quality/integrity. Unlike SLS/SLM parts, there is little or no published work regarding the effects of LP on intricate surfaces generated using the DM process. Hence the focus and motivation of the present research was to investigate the influence of key LP operating parameters and process environment on the surface integrity of DM printed stainless steel workpieces as well as an in-depth spectroscopic analysis of oxide layer formation.

3. Experimental work

3.1. Design of experiments for LP parameter optimisation

The initial laser polishing parameter optimisation experiments were carried out on planar, cube shaped stainless steel (SS316L) specimens produced using the DM process. Table 2 details the nominal composition of the printed workpiece material, which has a melting temperature of 1538°C [45]. All of the LP trials were conducted on a laser micromachining system utilising a MOPA-based Yb-doped fibre nanosecond (ns) laser source with a maximum average power of 50 W and wavelength (λ) of 1064 nm. The system was equipped with a 100 mm telecentric lens, a 3D scanhead (RhoThor RTA) mounted on a Z-axis stage with a maximum linear speed of 2.5 m/s and a stack of four stages (2 rotary and 2 linear) for positioning of workpieces within the machine's working envelop. Average laser power (P) and pulse duration (t) were kept constant at 37.2 W and 220 ns respectively with a single polishing pass carried out in normal atmospheric conditions for all tests. A full factorial experiment involving a total of 75 tests without any blocking or replication was performed to investigate the effect of varying laser fluence (energy density) together with the pulse overlap along the scanning direction/machine X-axis (determined by the scanning speed and pulse frequency) and step-over direction/machine Y-axis (determined by the hatching pitch) on workpiece surface roughness. The LP parameter levels for each of the variable parameters are detailed in Table 3. Analysis of variance (ANOVA) was used to identify the significant factors and interactions. A preliminary study was undertaken to identify the suitable ranges of energy density and X and Y pulse overlaps [46].

The fluence and pulse overlap values were calculated using Eqn. 1 to 5. The Rayleigh length (Z_R) was initially determined from Eqn. 1 followed by the Gaussian beam radius (w_z) using Eqn. 2:

$$Z_R = \frac{\pi(w_0)^2}{\lambda} \quad \ldots (1)$$

$$w_z = w_0\sqrt{1+\left(\frac{Z}{Z_R}\right)^2} \quad \ldots (2)$$

where:

w_0 - beam radius at the focal plane (29.5 µm, measured with a beam profiler)

The fluence/energy density (E_d) was then calculated using Eqn. 3:

$$E_d = 2\frac{P/f}{\pi(w_z)^2} \quad \ldots (3)$$

while the overlap factors along X and Y were ascertained using Eqn's. 4 and 5 [47], respectively:

$$OP_x = \left(1-\frac{v/f}{D+vt}\right)\times 100 \quad \ldots (4)$$

$$OP_y = \left(1-\frac{p}{D}\right)\times 100 \quad \ldots (5)$$

where,

v - beam scanning speed along X, varied between 900 to 5500 mm/s;

f - pulse frequency, varied between 30000 to 50000 Hz;

D - beam spot diameter at the focal plane (59 µm, measured with a beam profiler);

p - hatching pitch/step-over, varied between 3 to 11 µm.

3.2. Surface characterisation

Oxide layer formation on specimen surfaces during LP under air, argon and nitrogen gas environments was initially assessed. However, preliminary trials revealed that Ar was more efficient than N_2 at improving workpiece roughness and minimising surface oxidation. Therefore, only Ar was used in subsequent mainstream trials. The LP trials in argon were

conducted in a cylindrical aluminium chamber measuring 100 × 100 × 60 mm. The chamber was fitted with a toughened glass top lid that was transparent to the near infra red (NIR) laser beam while the Ar gas was delivered at a flow rate of 14 L/min and pressure of 8 bar.

Both qualitative and quantitative assessment of surface oxidation of the specimens polished in air and Ar were carried out using various techniques including X-ray energy dispersive spectroscopy (EDX), X-ray photoelectron spectroscopy (XPS) and glow discharge optical omission spectroscopy (GDOES). In order to confirm the presence of oxygen on the polished surfaces, EDX was carried out using an Oxford Inca 300 system coupled to a JEOL 6060 scanning electron microscope (SEM). This was followed by XPS measurements performed using a Kratos Ultra DLD fitted with a monochromated Al k alpha source emitting X-rays at 1486.7 eV in order to quantify the percentage of elements oxidised in the surface and sub-surface of the LP specimens. For a wide scan, the source operated at 75 W and the detector was set to sweep between 1100 and 0 eV with a 1 eV step size and pass energy of 160 eV. Region scans were undertaken simultaneously with the source running at 200 W, the detector sweeping at a step size of 0.1 eV and pass energy of 20 eV. All measurements were conducted at a pressure of 5×10^{-9} mbar. In order to remove the carbon from the samples' top layers, Ar ions were sputtered over an area of 4×4 mm^2 for 27 min with 4 kV and an emission current of 8 mA. To evaluate the depth of the oxide layers, GDOES analysis was further carried out on a SPECTRUMA ANALYTIK GmbH system (model number GDA650HR), with argon as the plasma excitation source and a chamber gas pressure of 250 Pa. A power of 10 W was used in a pulsed radiation frequency (RF) mode with a frequency of 2.2 kHz, on-duty ratio of 30% and spot diameter of 2.5 mm.

The presence of thermodynamically stable phases in SS316L at ambient temperature and following LP was evaluated using Thermo-Calc software. Relevant thermodynamic properties were calculated using information from databases for the selected materials, which

was primarily TCFE7 covering various steel alloys, together with TCOX5 and SSUB5 for other elements present in the workpiece [48]. The results for the formation of oxide compounds obtained with Thermo-Calc software were verified against X-ray diffraction (XRD) data obtained using a Siemens D5000 diffractometer with a Cu target (wavelength, λ = 54 picometre). The samples were continuously scanned with the detector rotating from 12° to 100°, at a step size of 0.05° and time per step of 0.2 s. The data was subsequently analysed with the EVA software and the peaks were identified by comparing the results to standard databases (JCP) within the software.

An Alicona G5 InfiniteFocus system employing 'Focus Variation' (FV) technology was utilised to perform 3D surface topography evaluation of the as-received and laser polished DM parts. A 50X optical magnification with lateral and vertical resolutions of 1.5 µm and 40 nm respectively were used for all measurements. The captured data was assessed in terms of areal surface parameters encompassing S_a (arithmetic mean deviation of the surface), S_t (total height of the surface) and S_z (10-point height of the surface) together with surface defects. High resolution / magnification micrographs of the LP surfaces were also recorded using the SEM.

As laser processes involve surface melting and re-solidification, formation of a heat affected zone (HAZ) is expected and thus in order to control the material behaviour, microhardness assessment of the LP surfaces was carried out. The samples' cross-sections were hot mounted in edge retentive bakelite, further ground and polished using SiC paper on a Buehler grinder-polisher. The microhardness measurements of the specimens (depth profile) were conducted on a Mitutoyo HM-124 microhardness tester with a load of 25 g and indent time of 15 s. The average value of ten measurements, each taken at 10 µm intervals from the polished surface until the bulk hardness achieved, was calculated and plotted. The centre point of the indents was kept at a minimum distance of 30 µm from each other in order

to minimise the influence of previous indents on the new reading. The SS316L samples were subsequently immersion etched in Glyceregia solution (15 mL glycerol, 10 mL HCl and 5 mL HNO_3) for 5 to 10 mins, with corresponding microstructural analysis performed using a Leica optical microscope and SEM.

3.3. Laser polishing of 3D printed structured SS316L parts

Laser polishing of structured DM SS316L parts having as-received roughness levels of 2.4-3.0 µm S_a were carried out utilising the optimised LP settings. The component design is shown in Fig. 3. Equivalent settings were also employed for the LP of semi-polished / intermediately polished (deburring by vibratory polisher, followed by manual polishing) SS aesthetic parts with a base roughness of S_a=~0.43-0.49 µm. As with the planar workpieces, the resulting surface roughness of the structured DM parts following LP were analysed using FV technology.

4. Results and discussion

4.1. Optimisation of LP parameters

The main effect plots of laser fluence and pulse overlap factors along X and Y on workpiece S_a, S_t and S_z are shown in Fig. 4. Mean S_a, S_t and S_z improved with the increase of energy density from 5 to 9 J/cm^2 and also with the increase of both OP_x and OP_y from 82% to 95%. The interaction plots for E_d and OP_x and E_d and OP_y are shown in Fig. 5(a) and 5(b) respectively. As it can be seen in the figure, mean S_a remained almost unchanged at the highest OP_x and OP_y levels irrespective of the fluence levels. With the reduction in the overlapping ratio, mean S_a typically decreased with the increase of laser energy density. The interaction plot between OP_x and OP_y in Fig. 5(c) showed that OP_y should be set in the range from 88 to 91% if a 95% OP_x is utilised in order to achieve the best areal surface roughness.

The interaction plots for E_d, OP_x and OP_y with regard to S_t and S_z are detailed in Figs. 6 and 7 respectively. Typically, the trends are similar to that for S_a in Fig. 5 and the best surface finish was achieved with a fluence of 9 J/cm^2 and overlap factors between 88-91% for both X and Y. An ANOVA for S_a including two-way interactions between the factors was carried out with the results given in Table 4. The OP_x parameter had the highest influence on surface roughness with a percentage contribution ratio (PCR) of 49.89. This was followed by the combined effect of E_d and OP_x (PCR=12.53) and the sole effect of fluence (PCR=12.2). The contributions of OP_y and the interaction between OP_x and OP_y to the average surface roughness were comparable, i.e. PCRs of 9.28 and 8.36, respectively. Although all factors and their interactions were statistically significant at 5% level, pulse overlap along the beam scanning direction (X) was found to be the most important contributing factor in improving the surface quality. This can be explained with the bigger overlapping range considered in the factorial design.

Figure 8 shows representative 3D topographies of an as-received sample together with LP surfaces obtained using various process settings. Tiny lumps on the LP surface in Fig. 8(b) suggest that minuscule ablation together with surface re-melting might have taken place when the overlapping was 95% in both X and Y directions. This could be explained with high accumulated thermal energy generated at these processing conditions. With the reduction of OP_y to 85%, surface finish improved by approximately 96% compared to the parent material (S_a reduced from 3.78 to 0.14 µm), however step-over marks were visible as depicted in Fig. 8(c). Further reduction of OP_x and OP_y led to the formation of pits/holes on the surfaces as shown Fig. 8(d), as well as a higher surface roughness of 1.73 µm S_a, which indicates lower heat absorption and consequently insufficient melting of the material.

Areal topographies of LP stainless steel surfaces with fluence of 9 J/cm^2 together with varying OP_x and OP_y are shown in Fig. 9. Several lumps and redeposited material are visible

in Fig. 9(a), which suggests a combination of ablation and surface overmelting (SOM) occurred at the highest LP process settings (E_d: 9 J/cm^2, OP_x and OP_y of 95%), due to a greater amount of accumulated thermal energy in the material. This is also reflected in the higher roughness of 0.35 µm S_a. The LP regime changed to surface shallow melting (SSM) when the overlapping factor along the hatching direction was reduced to 88%, which led to a reduction of S_a to 0.19 µm as shown in Fig. 9(b). However, further reductions in both OP_x and OP_y resulted in step-over marks and a lower heat accumulation, and ultimately an increase of S_a to 0.55 µm, as illustrated in Fig. 9(c). Thus, it can be inferred that surface shallow melting is preferable to achieve the best results in terms of surface quality. The optimum / recommended LP parameters for the DM SS316L workpieces identified in this research are a laser fluence of 9 J/cm^2 together with an overlap factor of 91-95% for both the scanning and step-over directions. However, if OP_x is set at its highest level, OP_y should be reduced to 88-91% in order to avoid exceeding the ablation threshold and SOM.

4.2. Surface characterisation

The resulting surfaces of the DM SS316L workpiece, laser polished under Ar gas environment at different fluence levels (9 - 20 J/cm^2), are shown in Fig. 10. The pulse overlaps along X and Y were kept constant at 95% and 91% respectively based on the optimisation results in Section 4.1. The corresponding SEM micrographs of surface topography outlined in Fig. 11 clearly show that both ablation and SOM occurred when operating at the highest level of fluence (20 J/cm^2) in argon. The cauliflower-like globular surface morphology suggests that excessive heating and subsequent cooling took place with a high gradient. Similar laser-material interaction was observed in trials with E_d down to 16 J/cm^2, but which switched to surface re-melting/SSM when E_d was below 13 J/cm^2. The visual appearance of the processed surfaces also changed from black/dark brown to shinny

metallic with the decrease of fluence from 20 to 9 J/cm^2. Furthermore, Fig. 11(c) shows the presence of entrapped gas bubbles and pores on the surface, which were absent on specimens polished in air using equivalent laser settings, see Fig. 11(d).

As all of the specimens polished in air exhibited black or dark brown surfaces it was inferred that this happened due to oxidation, which was similarly reported in the literature [1, 28, 35]. An EDX area mapping (Fig. 12(b)) and line scan (Fig. 12(c)) at the junction of a LP region and parent DM SS316L surface proved that surface oxidation took place, where the oxygen content was 26.3 wt% in the processed area compared to only 0.8 wt% in the base material. The results of EDX spot analysis are provided in Table 5.

The XPS analysis carried out on the LP surfaces under atmospheric and Ar conditions showed that the outermost layer was contaminated with carbon. This was evidently reduced after ion etching the specimens for 27 min up to a depth of ~22 nm. Similar observation was reported by Vaithilingam et al. [1] when LP SLM Ti-6Al-4V parts. The presence of oxygen was also confirmed by this analysis. In addition, the XPS analysis revealed that the percentages of oxidised iron and chromium decreased at the sputtered depth of 22 nm and similarly with the reduction in energy density for the specimens polished in Ar. In contrast, all specimens polished in air exhibited 100% oxidation of Fe, Cr, Ni and Mo at the surface irrespective of the fluence settings. Following ion etching, only a part of the Fe and Ni oxides were removed, leaving the Cr and Mo phases completely oxidised. The results are summarised in Table 6 while the XPS spectra for Fe and Cr at the depth of 22 nm of the sample LP in Ar are provided in Fig. 13.

In order to validate results from the microscopy and spectroscopy analyses, four additional specimens were laser polished under atmospheric and argon conditions to assess process repeatability with respect to achievable surface roughness/quality, and to ascertain the thickness of the oxide layer using depth profile GDOES analysis. The images of the LP

surfaces shown in Fig. 14 were consistent with results obtained previously. The surface processed in air (S1) at E_d=20 J/cm^2 was black/dark brown, while those polished (S2a and S2b) at a reduced energy density of 9 J/cm^2 were light brown and the one treated in Ar environment (S3) exhibited silvery/shinny metallic surface. The combined ablation/SOM regime in S1 led to an increase of S_a, ranging from 5.9 to 6.4 µm, in comparison to the as-received specimen (3.2 µm S_a), whereas the SSM regime for S2a and S2b rendered a reduction in roughness by approximately 82-92% (S_a varied from 0.23 to 0.52 µm). The S3 specimen also showed similar decrease in S_a by 90-92% with values ranging between 0.25 to 0.29 µm. Representative Alicona images of LP surfaces are shown in Fig. 15. Hence, it can be inferred that the LP domain were properly identified and the process proved to be highly repetitive on DM SS316L workpieces.

The high surface roughness of S1 prevented the use of GDOES analysis which was only performed on the samples polished at E_d of 9 J/cm^2 (S2a and S3). Figure 16 clearly shows a difference in the oxygen profiles obtained between the specimens polished in air and argon. While the former exhibited an oxide layer with a depth of up to ~0.4-0.5 µm (Fig. 16(a)), the presence of oxygen was minimal in the latter case (Fig. 16(b)). It was further revealed that there was a segregation of Fe and Cr phases up to ~0.4 µm depth of the S2a specimen with an iron rich oxide in the outer sub-surface layer; however this phenomenon was not observed in the S3 specimen. Hence, it can be inferred that the Fe and Cr phases were predominantly oxidised when LP was carried out in air [49]. Similar observations were reported by Betz et al. [50], where the oxidation process of SS304 stainless steel was investigated at various temperatures. It was suggested that the formation of a Fe rich oxide outer layer was due to faster FeO formation compared to that of Cr_2O_3 and other Fe oxides. Trigwell and Selvaduray [51] also studied the oxide surface layer of SS316L after welding and concluded that the

discoloured region was composed of a Fe rich oxide and attributed its formation to the rapid growth kinetics of iron oxide.

An isothermal section of the Fe-Cr-O system at 1461°C (theoretical melting temperature of SS316L) was determined by using the Thermo-Calc software, that indicated the formation of stable spinel phases (general formula AB_2O_4 where A and B are the divalent and trivalent metal ions, respectively) at high temperatures. This was further confirmed with the XRD analysis (Fig. 17) that showed the presence of spinel phases, Fe_3O_4 and $FeCr_2O_4$ in the spectra while the black triangles represent FCC structure of austenitic stainless steel. Formation of spinel phases during high temperature oxidation of SS316L in air plasma was also reported by Vesel et al. [52]. Additionally, the outer surface layer of the LP specimen processed in argon was more crystalline compared to that of the samples processed in air. A sharp peak in the XRD spectra of S3 in Fig. 18 supports this observation.

Figure 19(a) displays microhardness depth profiles of laser polished specimens in air and argon environments. The sample polished with higher energy density typically exhibited greater sub-surface microhardness (of up to ~50-60%) until a depth of ~90-100 μm than those processed with lower thermal energy. The average hardness of S1 was between 280-290 $HK_{0.025}$ within 50 μm from the top layer with the maximum value reaching up to ~318 $HK_{0.025}$, whereas that of the other three specimens (polished at 9 J/cm^2) generally varied between 210-255 $HK_{0.025}$ within 50 μm depth. The data is also supported by the representative microhardness indentation marks on the cross-sections of S1 and S2a, shown in Fig. 19(b), that exhibit greater long axis dimensions up to a depth of 90-100 μm in the latter specimen resulting in lower hardness values than S1. The increase in microhardness in S1 compared to S2a, S2b and S3 was due to the greater sub-surface hardening effect caused by the higher energy input in this specimen [13]. Kruth et al. [2] also observed increase in hardness values following laser re-melting with higher laser power (i.e. greater thermal load)

when LP of SLMed stainless steel parts. The sub-surface microhardness of the samples LP at lower fluence (S2a, S2b and S3) were still higher than the bulk hardness (~170 $HK_{0.025}$), which was a result of the reduction in porosity and a more densified sub-surface following LP. Kruth et al. [2] and Lamikiz et al. [37] also reported an increase in hardness and densification at the re-melted zone. The current investigation however did not reveal any apparent change in sub-surface microhardness due to variation in process environment (air or argon). From Fig. 19(a), the depth of affected layer was estimated as ~90-100 μm at which the bulk hardness (~170 $HK_{0.025}$) was achieved for all specimens. This was also supported by the un-etched cross-sectional micrographs of S1 and S3 (Fig. 20), where sub-surface layer contamination and a higher porosity were observed up to a depth of 90-100 μm in the former specimen (Fig. 20(a) and 20(b)) while a dense sub-surface morphology with minimal porosity was seen in the latter sample (Fig. 20(c) and 20(d)). The observation clearly reveals that a combination of ablation and SOM were the dominant laser material interaction regime when performing LP with a higher energy density. Conversely, all other LP specimens processed with lower fluence settings exhibited SSM as the dominant process regime as indicated by the smooth top surface layers. Similar results were also observed on the etched specimens. While the S1 sub-surface was evidently rougher with visible oxides, lumps, holes, pits and irregularities (Fig. 21(a)), the S3 sample was comparatively smoother with virtually no sign of oxide layers (Fig. 21(b)). Following the argument on the estimated depth of the affected layer, shown in Fig. 19, the same can also be assessed from Fig. 21(a), where no distinguishable grain structures were observed up to a depth of ~100 μm. Nevertheless, the bulk microstructure of all samples exhibited an austenitic phase with twin grain boundaries together with the presence of a secondary sigma phase (δ-ferrite).

4.3. Laser polishing of 3D printed structured SS316L parts

The identified LP domain in Section 4.1 was employed to process complex surfaces on DM SS316L parts as shown in Fig. 22(a), with an initial roughness of S_a=2.4 μm. The LP surfaces exhibited approximately 90% reduction in S_a, down to 0.25 μm, similar to the results in Sections 4.1 and 4.2, together with a decrease in S_t and S_z from 38.2 and 33.9 μm to 2.3 and 2.14 μm, respectively. The stair-step effect, which is an inherent issue in 3D printed parts, was also minimised following the LP operation as shown in Figs. 22(b) and 22(c). Furthermore, the roughness of the polished surfaces was isotropic (similar roughness values in all directions), which suggests improvements in the fatigue life of the parts due to the minimised risk of crack nucleation [37].

The same LP settings were also applied for processing of semi-polished free form surfaces on aesthetic parts with roughness in the range of 0.4 to 0.5 μm. The S_a of the LP surfaces varied from 0.12 to 0.23 μm, which represented a roughness reduction of 50 to 75%, whereas S_t decreased by approximately 80-90%, from initial values of 9.77 to 17.71 μm to 1.5 to 2.3 μm after LP. Figure 23(a) shows the 3D topography of an intermediately polished surface whereas Figs. 23(b) and 23(c) depict the LP regions. Thus, the level of improvement depends on the initial as-received surface roughness, in particular the effectiveness of the LP process is enhanced with increase of the initial surface roughness [37]. The process was also proven to be applicable for surface functionalisation of miniaturised parts for mass production. A 10 x 10 mm^2 area was laser polished using the optimum processing setting in only 16 s.

5. Conclusions

- The study investigated the influence of main laser polishing parameters and process environment on the surface integrity of 3D printed stainless steel components. Energy

density and pulse overlap along the beam scanning direction were the most influential factors in improving the surface quality. A lower accumulated thermal energy resulted in insufficient melting while that beyond the optimised value led to ablation and surface over-melting of material. A maximum reduction in areal surface roughness of over 94% was achieved at the optimised LP settings with surfaces typically exhibiting isotropic roughness together with no signs of substantial scratch marks, pits, holes, lumps and irregularities as compared to the as-received samples. The optimised laser parameters were also successfully implemented for polishing DM SS316L structured parts as well as semi-polished stainless steel aesthetic components. The effectiveness of the LP operation however was largely dependant on the initial surface roughness of the workpiece; the higher was the initial roughness, the greater was the reduction in S_a.

- The colour intensity of the LP surfaces was found to be directly related to the amount / depth of the surface oxidation. The Fe and Cr were predominantly oxidised to form Fe_3O_4 and $FeCr_2O_4$ mixed spinel phases. Use of argon shielding significantly reduced the oxidation and thus is recommended if oxidation must be avoided following LP operations. However, laser-induced oxidation is desirable in certain applications (such as oxidation of titanium to form titanium oxides) and is one of the most reliable methods due to its controllability and selectivity. The technology utilises colour marking on the surfaces, achieved through generating oxide films of different thicknesses corresponding to specific laser parameter settings.
- Cross-sectional microstructure of LP specimens processed with higher laser energy density revealed a combination of ablation and SOM as the dominant laser material interaction regimes. This resulted in a sub-surface layer with a greater amount of porosity. Conversely, LP samples processed with a reduced fluence exhibited SSM as the primary polishing regime that led to a dense sub-surface area within approximately 100 µm depth

and minimal porosity. Sub-surface microhardness of the specimens polished with higher energy density was typically greater (of up to ~50-60%) up to a depth of ~90-100 μm compared to those processed at lower fluence settings. This was due to the larger thermal input and consequent more intense sub-surface hardening of the material. The microhardness of the specimens polished at a reduced fluence was still higher, up to a depth of ~100 μm, than the bulk value. This was a result of the reduction in porosity and a more densified sub-surface layer. Laser polishing in argon environment however did not show any change in microhardness compared to those processed in air but with equivalent fluence. The increase in hardness following LP can improve the wear resistance of the surface, while densification of sub-surface due to re-melting would eliminate any pores that are inherent to the parts fabricated via AM processes, thereby demonstrating the laser polishing technology beneficial to the applications where fully dense outer shell of the AM components is crucial.

Acknowledgements

The research was supported by two EC-funded projects via the FP7 NMP programmes on "High Performance Production Line for Small Series Metal Parts" (HYPROLINE, Grant Agreement No 314685) and "High throughput integrated technologies for multi-material functional Micro Components" (HINMICO, Grant Agreement No 609110). The work was also carried out within the framework of the INTERREG IVB NWE project ECO-efficient LASER technology for FACTories of the future (ECOLASERFACT) as well as a project sponsored by the Korean Government on "Laser-Based Modules for Functional Surface Texturing". The authors also acknowledge the support received by TNO, Netherlands, for providing the XPS facility, Ms. Josephine Magnusson of Digital Metal for carrying out the

Thermo-Calc calculation and Mr. Shaojun Qi from the School of Metallurgy and Materials, University of Birmingham, for operating the GDOES system.

References

[1] J. Vaithilingam, R.D. Goodridge, R.J.M. Hague,S.D.R. Christie, S. Edmondson, The effect of laser remelting on the surface chemistry of Ti6Al4Vcomponents fabricated by selective laser melting, J. Mater. Proc. Technol. 232 (2016) 1-8.

[2] J.-P. Kruth, E. Yasa, J. Deckers, Experimental investigation of laser surface re-melting for the improvement of selective laser melting process, 14èmes Assises Européennes du Prototypage & Fabrication Rapide, Paris, 2009, pp. 1-6.

[3] E.V. Bordatchev, A.M.K. Hafiz, O.R. Tutunea-Fatan, Performance of laser polishing in finishing of metallic surfaces, Int. J. Adv. Manuf. Technol. 73(1) (2014) 35-52.

[4] E. Willenborg, Polishing with laser radiation, in: R. Poprawe (Ed.), Tailored Light 2, Laser Application Technology, Springer-Verlag Berlin Heidelberg, 2011, pp. 196-202.

[5] C. Gu, Z. Jin, Y. Wang, R. Zhuang, X. Lu, S. Zhao, G. Zou, Polishing technology of surface for diamond film using the method of laser ablation, Chinese Sci. Bulletin 42(23) (1997) 2010-2013.

[6] S.M. Pimenov, V.V. Kononenko, V.G. Ralchenko, V.I. Konov, S. Gloor, W. Lüthy, H.P. Weber, A.V.Khomich, Laser polishing of diamond plates, Appl. Phys. A 69 (1999) 81-88.

[7] O.Y. Bol'shepaev, N.N. Katomin, Laser polishing of glass articles, Glass and Ceramics 54(5-6) (1997) 141-142.

[8] H.-Y. Wang, D. L. Bourell, J. J. Beaman Jr., Laser polishing of silica slotted rods, Mater. Sci. Technol. 19 (2003) 382-387.

[9] V.K. Sysoev, Science for glass production, Glass and Ceramics 60(3-4) (2003) 106-107.

[10] J. Hildebrand, K. Hecht, J. Bliedtner, H. Műller, Laser beam polishing of quartz glass surfaces, Physics Procedia 12 (2011) 452-461.

[11] S. Heidrich, A. Richmann, P. Schmitz, E. Willenborg, K. Wissenbach, P. Loosen, R. Poprawe, Optics manufacturing by laser radiation, Opt. Laser Eng. 59 (2014) 34-40.

[12] E. Brinksmeier, O. Riemer, A. Gessenharter, L. Autschbach, Polishing of structured molds, CIRP Ann. 53(1) (2004) 247-250.

[13] R. Avilés, J. Albizuri, A. Lamikiz, E. Ukar, A. Avilés, Influence of laser polishing on the high cycle fatigue strength of medium carbon AISI 1045 steel, Int. J. Fatigue 33 (2011) 1477-1489.

[14] R. Avilés, J. Albizuri, E. Ukar, A. Lamikiz, A. Avilés, Influence of laser polishing in an inert atmosphere on the high cycle fatigue strength of AISI 1045 steel, Int. J. Fatigue 68 (2014) 67-79.

[15] E. Ukar, A. Lamikiz, L.N. López de Lacalle, D. del Pozo, J.L. Arana, Laser polishing of tool steel with CO_2 laser and high-power diode laser, Int. J. Mach. Tools Manuf. 50 (2010) 115-125.

[16] E. Ukar, A. Lamikiz, S. Martínez, I. Tabernero, L.N. López de Lacalle, Roughness prediction on laser polished surfaces, J. Mater. Proc. Technol. 212 (2012) 1305-1313.

[17] M.T.C. Chow, E.V. Bordatchev, G.K. Knopf, Experimental study on the effect of varying focal offset distance on laser micropolished surfaces, Int. J. Adv. Manuf. Technol. 67 (2013) 2607-2617.

[18] F.E. Pfefferkorn, N.A. Duffie, J.D. Morrow, Q. Wang, Effect of beam diameter on pulsed laser polishing of S7 tool steel, CIRP Ann. 63(1) (2014) 237-240.

[19] C.-S. Chang, T.-H. Chen, T.-C. Li, S.-L. Lin, S.-H. Liu, J.-F. Lin, Influence of laser beam fluence on surface quality, microstructure, mechanical properties, and tribological results for laser polishing of SKD61 tool steel, J. Mater. Proc. Technol. 229 (2016) 22-35.

[20] W. Guo, M. Hua, P. Wai-Tat Tse, A.C.K. Mok, Process parameters selection for laser polishing DF2 (AISI O1) by Nd:YAG pulsed laser using orthogonal design, Int. J. Adv. Manuf. Technol. 59 (2012) 1009-1023.

[21] A.M.K. Hafiz, E.V. Bordatchev, R.O. Tutunea-Fatan, Influence of overlap between the laser beam tracks on surface quality in laser polishing of AISI H13 tool steel, J. Manuf. Proc. 14 (2012) 425-434.

[22] J.D. Morrow, Q. Wang, N.A. Duffie, F.E. Pfefferkorn, Effects of pulsed laser micro polishing on microstructure and mechanical properties of S7 tool steel, 9th Int. Conf. on Micro-Manuf. (ICOMM), 2014.

[23] Q. Wang, J.D. Morrow, C. Ma, N.A. Duffie, F.E. Pfefferkorn, Surface prediction model for thermocapillary regime pulsed laser micro polishing of metals, J. Manuf. Proc. 20 (2015) 340-348.

[24] M. Vadali, C. Ma, N.A. Duffie, X. Li, F.E. Pfefferkorn, Pulsed laser micro polishing: Surface prediction model, J. Manuf. Proc. 14 (2012) 307-315.

[25] E. Ukar, A. Lamikiz, S. Martínez, F. Estalayo, I. Tabernero, Laser polishing of GGG70L cast iron with 2D scan-head, Procedia Eng. 63 (2013) 53-59.

[26] T.L. Perry, D. Werschmoeller, X. Li, F.E. Pfefferkorn, N.A. Duffie, The effect of laser pulse duration and feed rate on pulsed laser polishing of microfabricated nickel samples, J. Manuf. Sci. Eng., ASME Transac. 131 (2009) 031002-1-7.

[27] A.M.K. Hafiz, E.V. Bordatchev, R.O. Tutunea-Fatan, Experimental analysis of applicability of a picosecond laser for micro-polishing of micromilled Inconel 718 superalloy, Int. J. Adv. Manuf. Technol. 70 (2014) 1963-1978.

[28] T.L. Perry, D. Werschmoeller, X. Li, F.E. Pfefferkorn, N.A. Duffie, Pulsed laser polishing of micro-milled Ti6Al4V samples, J. Manuf. Proc. 11 (2009) 74-81.

[29] M. Vadali, C. Ma, N.A. Duffie, X. Li, F.E. Pfefferkorn, Effects of laser pulse duration on pulse laser micro polishing, 7th Int. Conf. on Micro-Manuf. (ICOMM), 2012, pp. 291-297.

[30] C. Ma, M. Vadali, N.A. Duffie, F.E. Pfefferkorn, X. Li, Melt pool flow and surface evolution during pulsed laser micro polishing of Ti6Al4V, J. Manuf. Sci. Eng., ASME Transac. 135 (2013) 061023-1-8.

[31] F.E. Pfefferkorn, N.A. Duffie, X. Li, M. Vadali, C. Ma, Improving surface finish in pulsed laser micro polishing using thermocapillary flow, CIRP Ann. 62 (2013) 203-206.

[32] V.M. Yermachenko, Y.A. Vdovin, V.D. Mironov, N.V. Naumov, V.N. Petrovskiy, N.M. Prokopova, V.I. Polsky, P.S. Dzhumaev, V.L. Yakushin, Technology of polishing of titanium surface using the fiber - laser radiation, Laser Physics 20(6) (2010) 1537-1544.

[33] C. Nüsser, H. Sändker, E. Willenborg, Pulsed laser micro polishing of metals using dual-beam technology, Physics procedia 41 (2013) 346-355.

[34] J. Kumstel, B. Kirsch, Polishing titanium- and nickel-based alloys using cw-laser radiation, Physics procedia 41 (2013) 362-371.

[35] L.Giorleo, E. Ceretti, C. Giardini, Ti surface laser polishing: effect of laser path and assist gas, Procedia CIRP 33 (2015) 446-451.

[36] J.A. Remos-Grez, D.L. Bourell, Reducing surface roughness of metallic freeform-fabricated parts using non-tactile finishing methods, Int. J. Mater. Prod. Technol. 21(4) (2004) 297-316.

[37] A. Lamikiz, J.A. Sánchez, L.N. López de Lacalle, J.L. Arana, Laser polishing of parts built up by selective laser sintering, Int. J. Mach. Tools Manuf. 47 (2007) 2040-2050.

[38] E. Yasa, J.-P. Kruth, J. Deckers, Manufacturing by combining Selective Laser Melting and Selective Laser Erosion/laser re-melting, CIRP Ann. 60 (2011) 263-266.

[39] E. Yasa, J.-P. Kruth, Microstructural investigation of Selective Laser Melting 316L stainless steel parts exposed to laser re-melting, Procedia Eng. 19 (2011) 389-395.

[40] E. Yasa, J.-P. Kruth, Application of laser re-melting on selective laser melting parts, Adv. Prod. Eng. Mgt. 6 (2011) 259-270.

[41] S. Marimuthu, A.Triantaphyllou, M. Antar, D. Wimpenny, H. Morton, M. Beard, Laser polishing of selective laser melted components, Int. J. Mach. Tools Manuf. 95 (2015) 97-104.

[42] B. Rosa, P. Mognol, J.Y. Hascoet, Laser polishing of additive laser manufacturing surfaces, J. Laser Appl. 27 (2015) S29102.

[43] A brochure on Höganäs Digital Metal® 3D Printing Technology.

[44] D. Wang, Y. Liu, Y. Yang, Theoretical and experimental study on surface roughness of 316L stainless steel metal parts obtained through selective laser melting, Rapid Prototyping J. 22(4) (2016) 706-716.

[45] Digital Metal, Höganäs, Safety Data Sheet (2014) p. 15.

[46] D. Bhaduri, P. Penchev, S. Dimov, S.L. Soo, Improving the surface integrity of 3D printed stainless steel parts by laser polishing, 4M/ICOMM Conf. Proc., Milan, 2015, pp. 593-600.

[47] J. Sabbaghzadeh, M.J. Hamedi, F. Malek Ghaini, M.J. Torkamany, Effect of process parameters on the melting ratio in overlap pulsed laser welding, Metal. Mater. Transac. B 39B (2008) 340-347.

[48] "Themo-Calc", Available on: http://www.thermocalc.com/products-services/databases/thermodynamic (Accessed on 08.05.2015).

[49] N. Birks, G. H. Meier, F. S. Pettit, Introduction to the High Temperature Oxidation of Metals, 2nd Ed., Cambridge University Press, 2006, ISBN: 9780521480420.

[50] G. Betz, G. Wehner, L. Toth, Compostion-depth profiles obtained with Auger electron spectroscopy of air oxidized stainless steel surfaces, J. App. Phys. 45 (1974) 5312-5316.

[51] S. Trigwell, G. Selvaduray, Effects of welding on the passive oxide film of electropolished 316L stainless steel, J. Mater. Proc. Technol. 166(1) (2005) 30-43.

[52] A. Vesel, M. Mozetic, A. Drenik, N. Hauptman, M. Balat-Pichelin, High temperature oxidation of stainless steel AISI316L in air plasma, Appl. Surf. Sci. 255 (2008) 1759-1765.

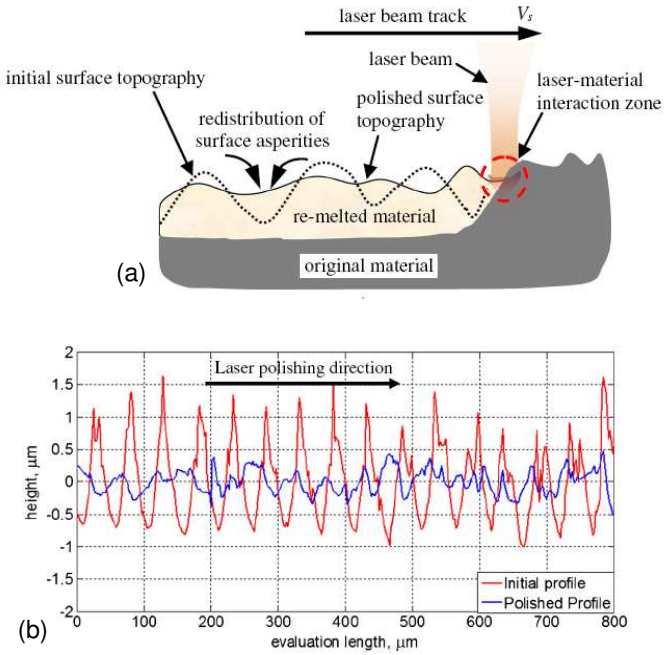

Fig. 1 (a) Schematic view of the re-melting mechanism, and (b) effect of laser irradiation on surface asperities [3]

Fig. 2 Process diagram showing the Digital Metal® technology [43]

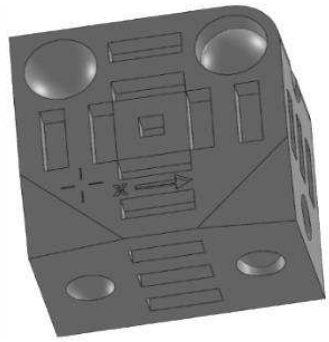

Fig. 3 CAD model of the DM SS316L part with overall dimensions of 10 × 10 × 10 mm

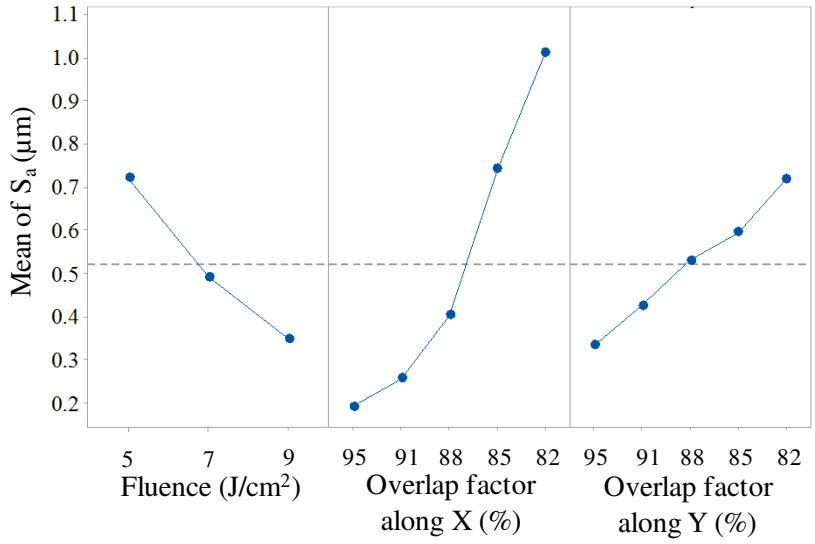

(a)

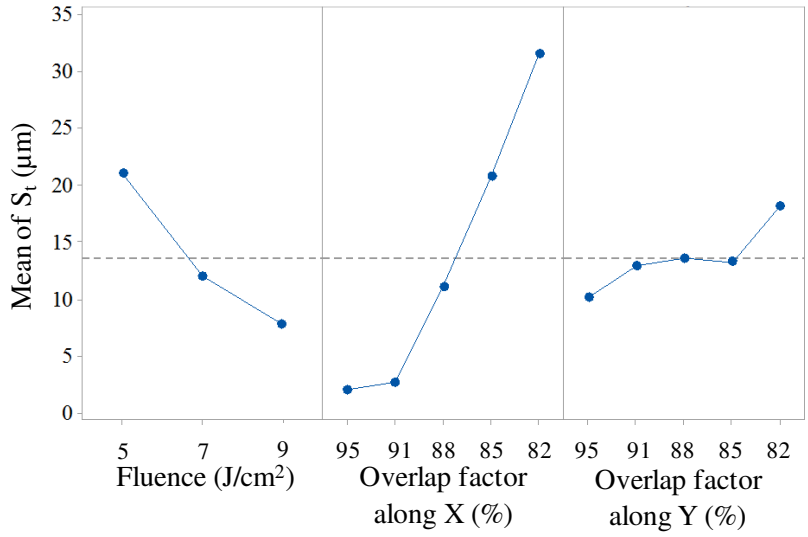

(b)

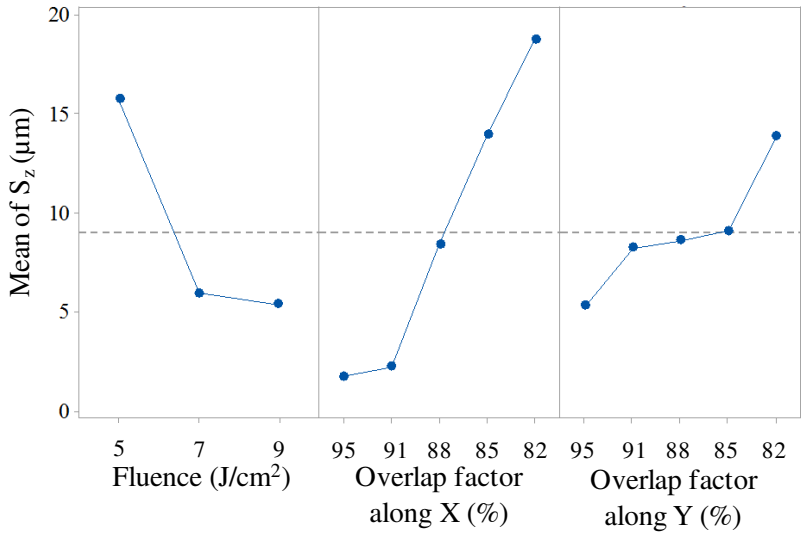

(c)

Fig. 4 Main effect plots for specimen roughness; (a) S_a, (b) S_t and (c) S_z

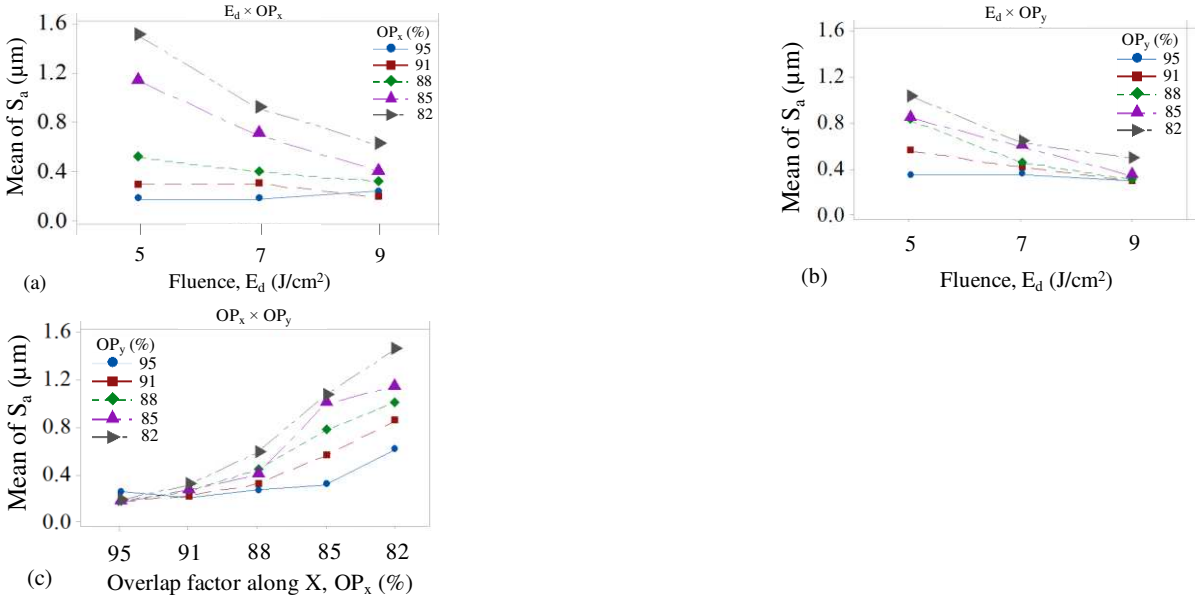

Fig. 5 Interaction plots of fluence and pulse overlap factors for S_a

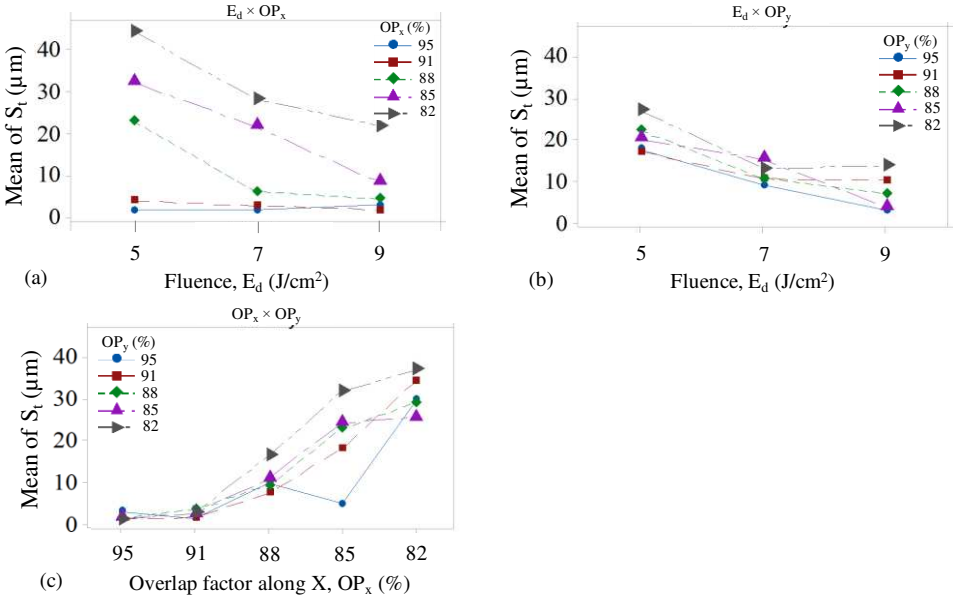

Fig. 6 Interaction plots of fluence and pulse overlap factors for S_t

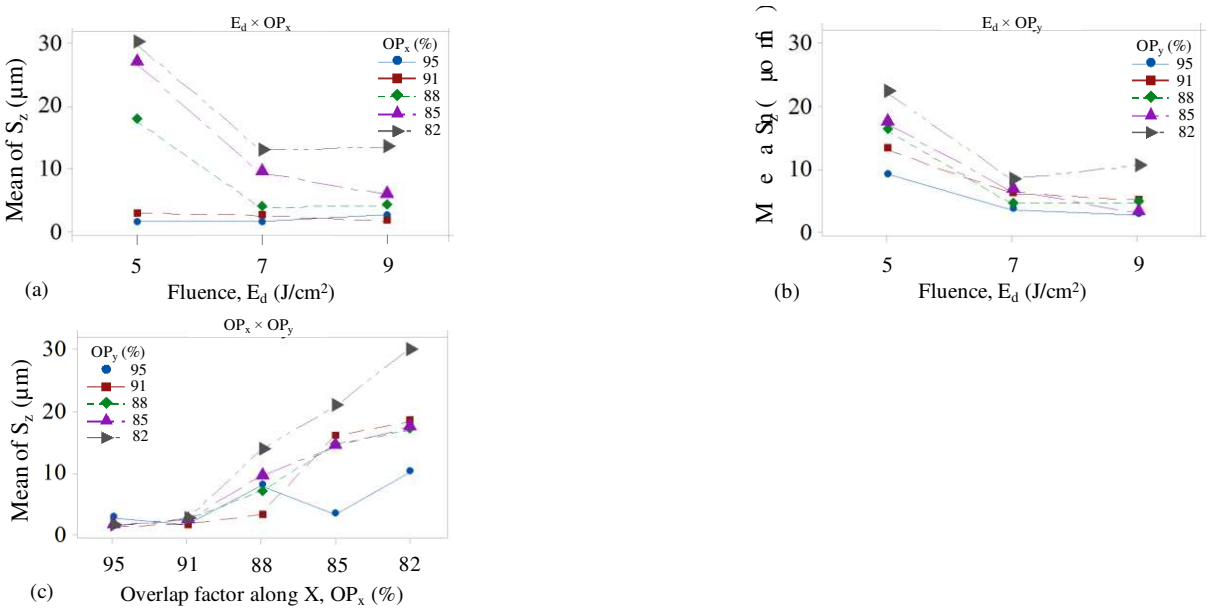

Fig. 7 Interaction plots of fluence and pulse overlap factors for S_z

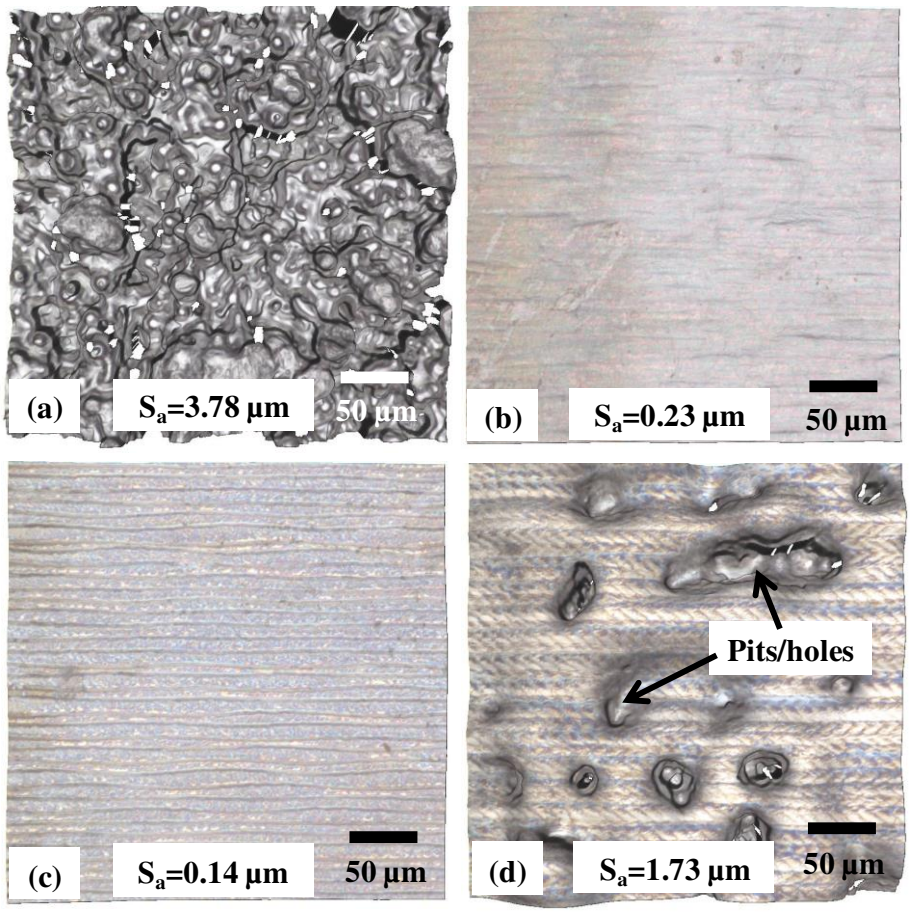

Fig. 8 Areal surface topographies of: (a) parent material; (b) LP areas processed at E_d: 5 J/cm^2, OP_x: 95%, OP_y: 95%; (c) E_d: 5 J/cm^2, OP_x: 95%, OP_y: 85%, (d) E_d: 5 J/cm^2, OP_x: 82%, OP_y: 85%.

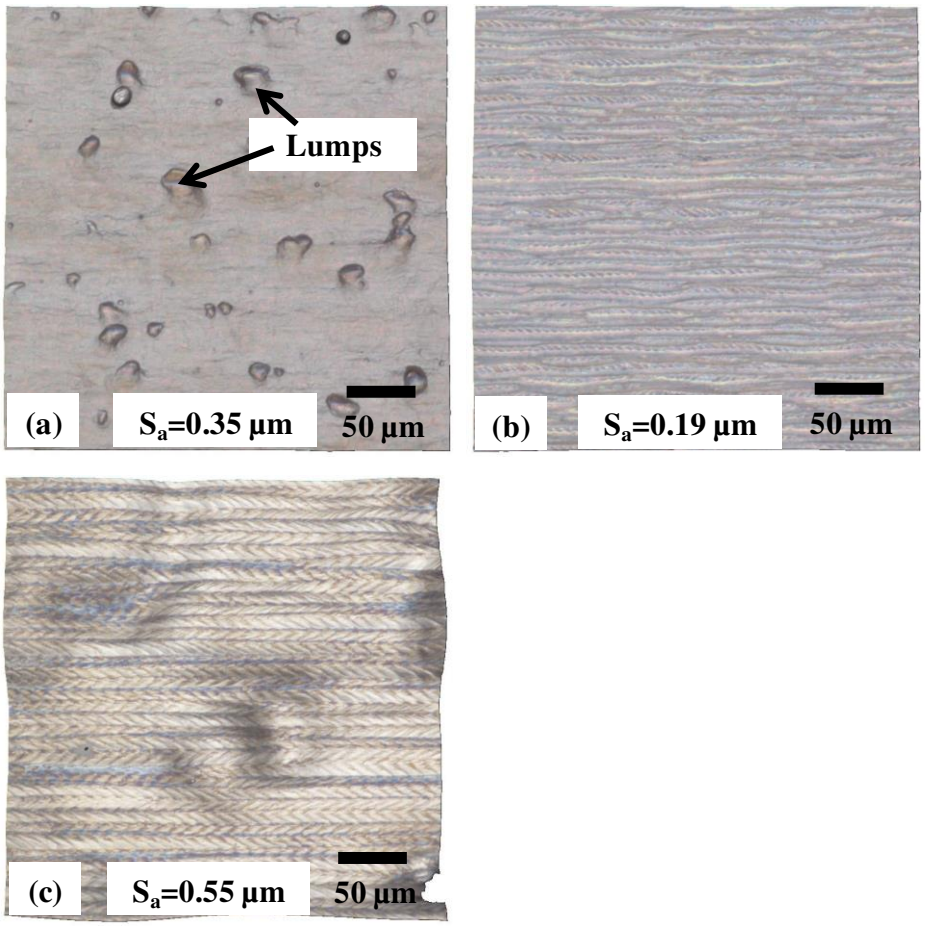

Fig. 9 Areal surface topographies of LP areas processed with: (a) E_d: 9 J/cm^2, OP_x: 95%, OP_y: 95%; (b) E_d: 9 J/cm^2, OP_x: 95%, OP_y: 88%; (c) E_d: 9 J/cm^2, OP_x: 82%, OP_y: 85%.

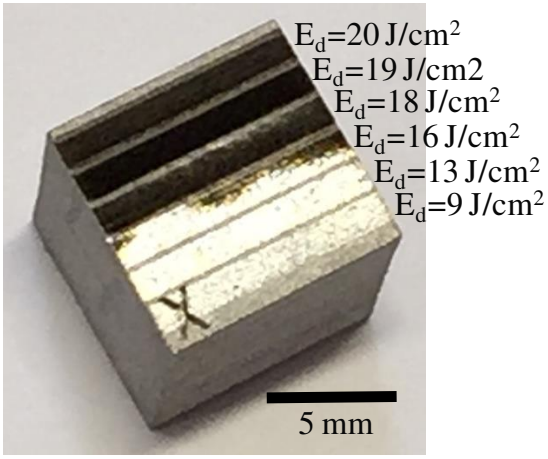

Fig. 10 Laser polished SS cube under Ar gas environment at different fluence levels

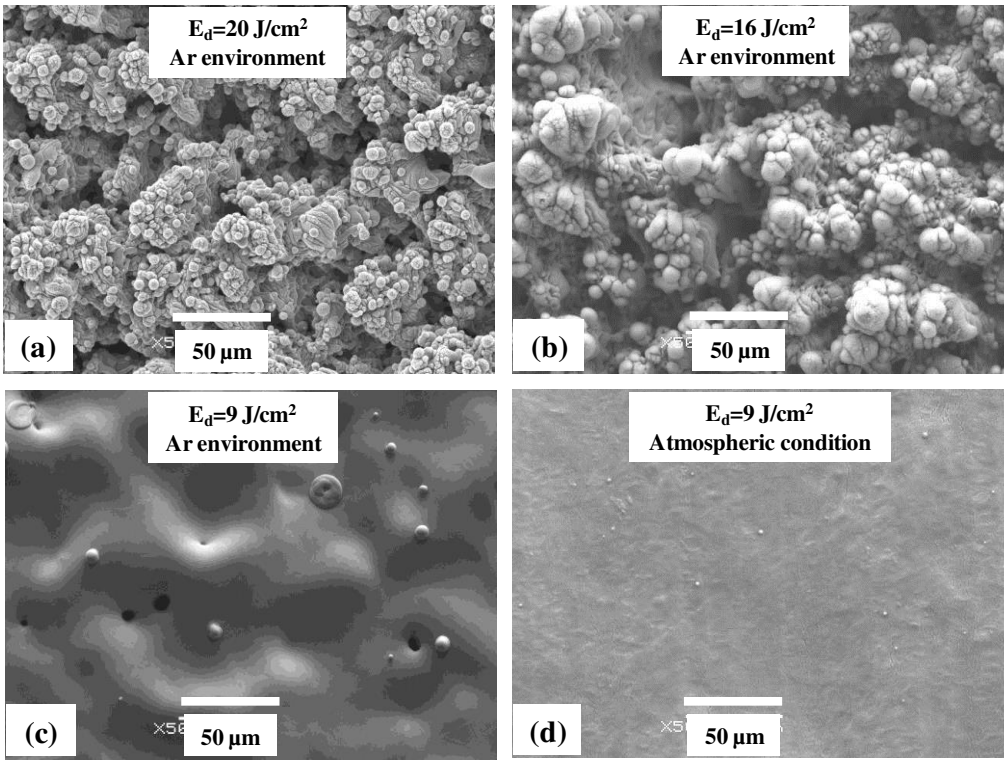

Fig. 11 Scanning electron micrographs of LP surfaces at fluence of: (a) 20 J/cm^2; (b) 16 J/cm^2; (c) 9 J/cm^2 under Ar environment; and (d) 9 J/cm^2 in air.

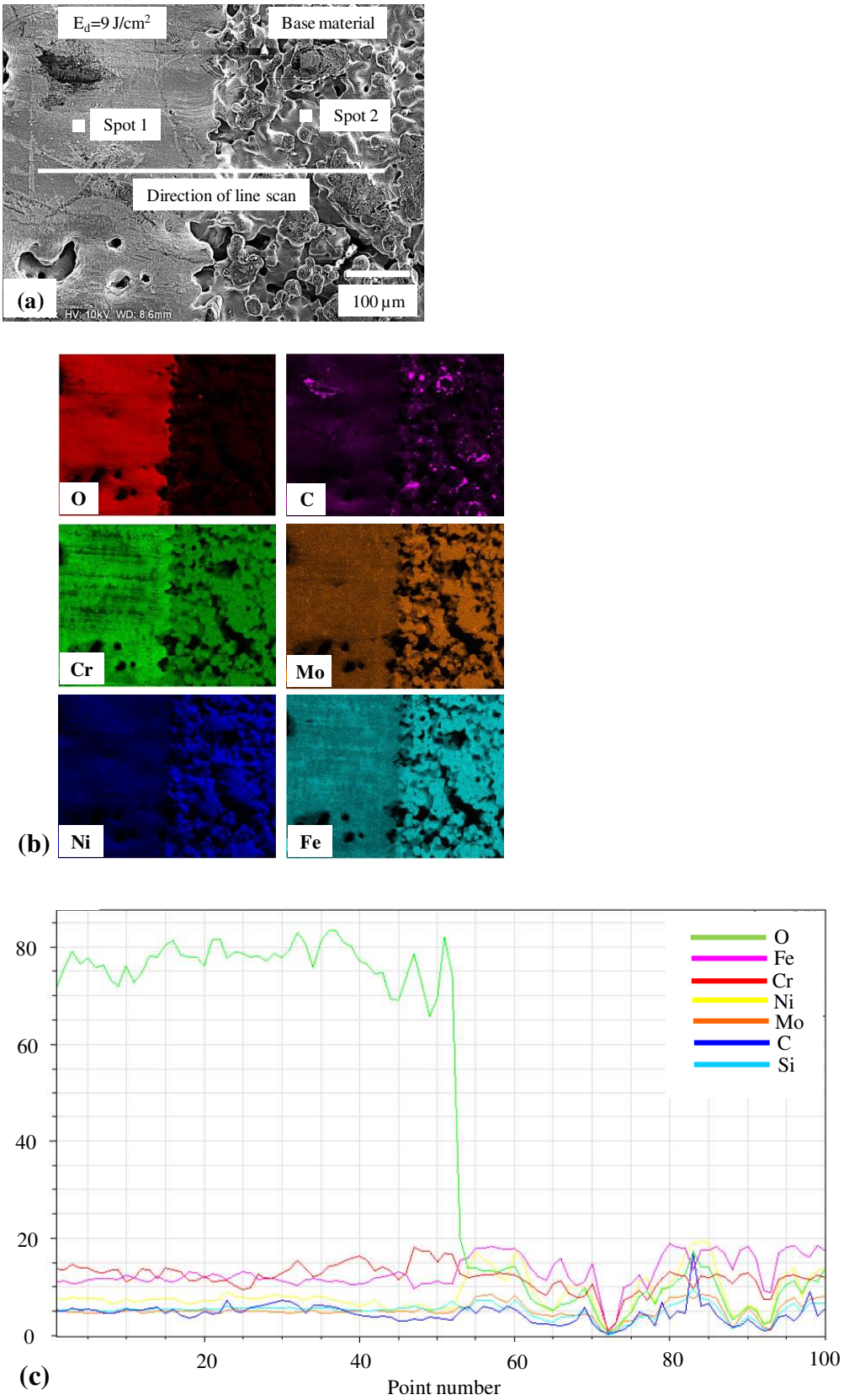

Fig. 12 (a) SEM micrograph of a junction between LP area and base material; (b) EDX area mapping; (c) EDX line scan.

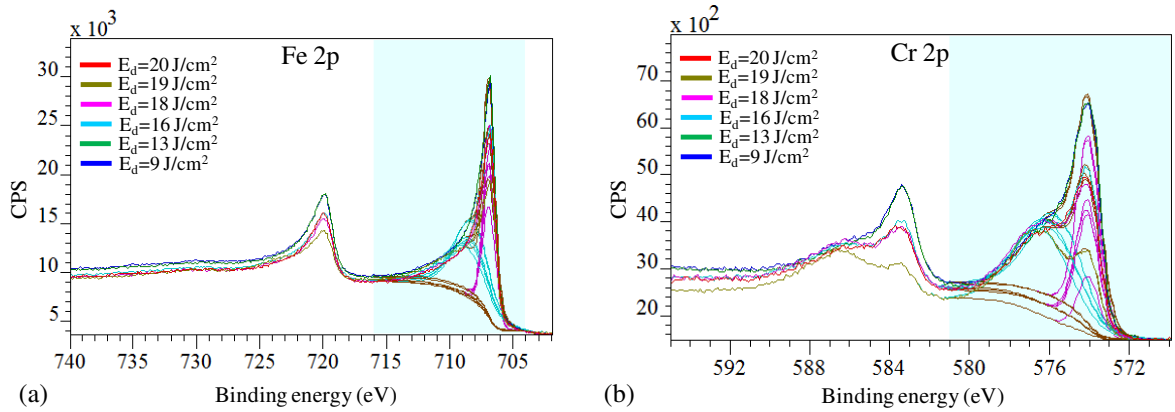

Fig. 13 XPS spectra of (a) Fe, (b) Cr at the depth of 22 nm of the specimen LP in argon

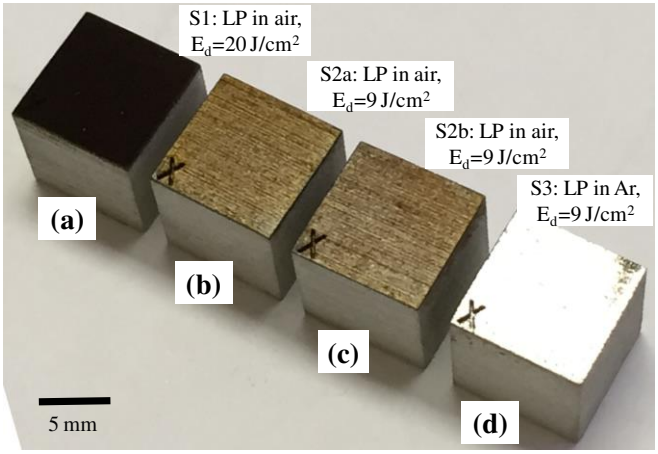

Fig. 14 Images of SS cubes S1, S2a and S2b laser polished in air at fluence of (a) 20 J/cm^2, (b)-(c) 9 J/cm^2 and (d) S3 in argon at 9 J/cm^2

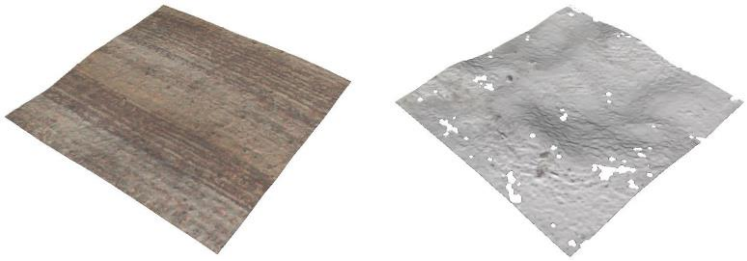

(a) S_a= 0.23 µm (b) S_a= 0.25 µm

Fig. 15 Laser polished surfaces in: (a) air (sample S2a); (b) argon (sample S3), (area: 325×325 µm).

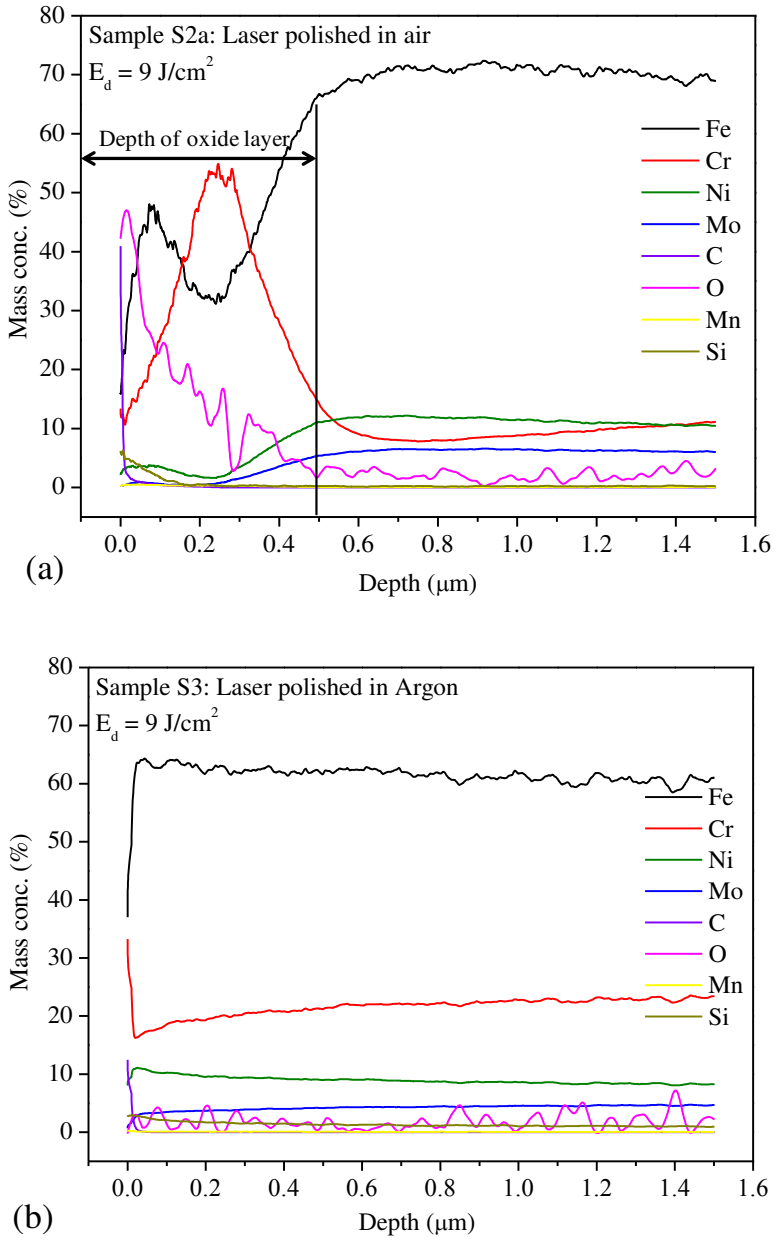

Fig. 16 GDOES analysis for specimens polished in: (a) air; (b) argon environment.

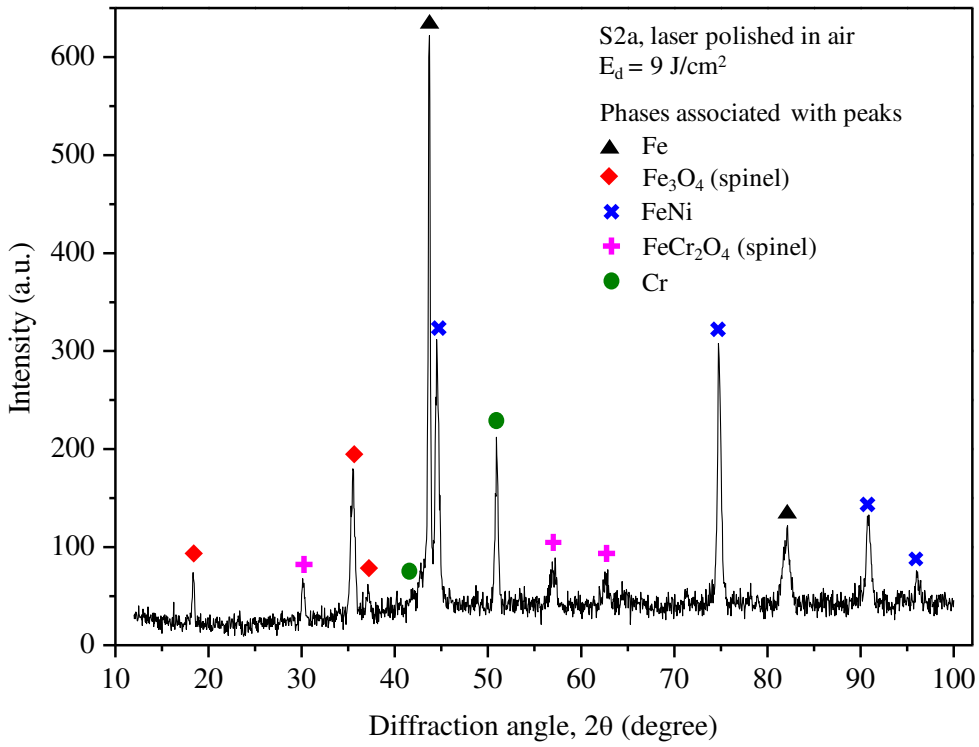

Fig. 17 X-ray diffraction spectra of the S2a specimen showing the presence of spinel phases

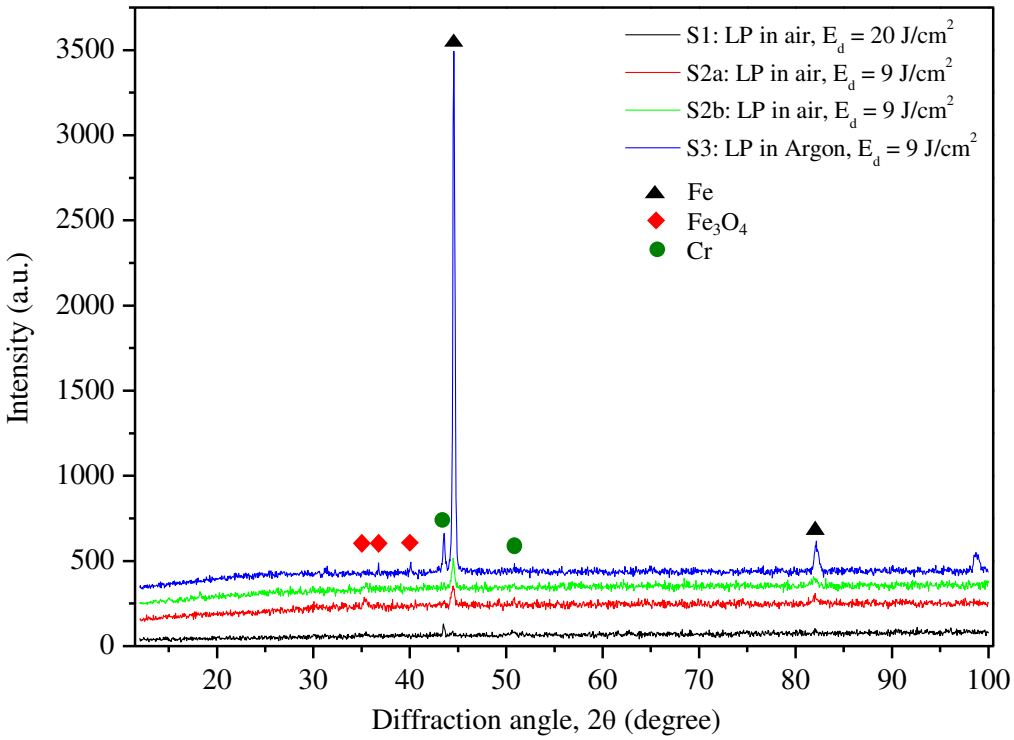

Fig. 18 X-ray diffraction spectra of the LP specimens processed in air and argon

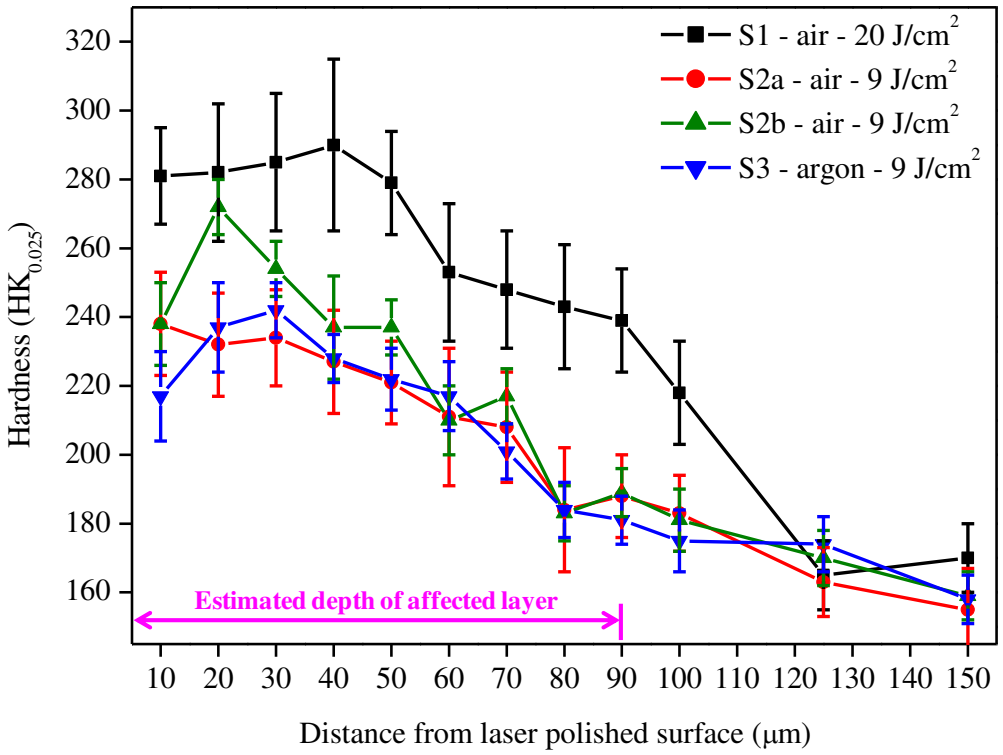

(a)

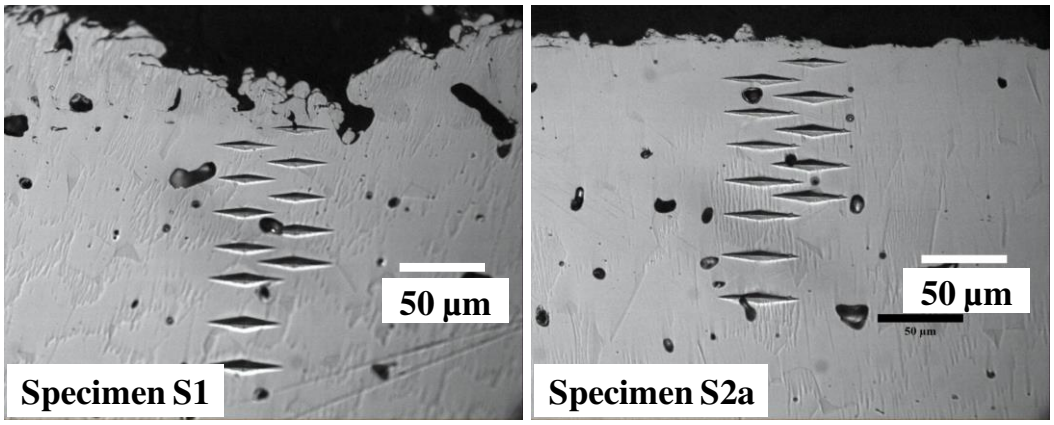

(b)

Fig. 19 (a) Microhardness depth profiles of LP specimens in air and argon, (b) representative microhardness indentations on samples S1 and S2a

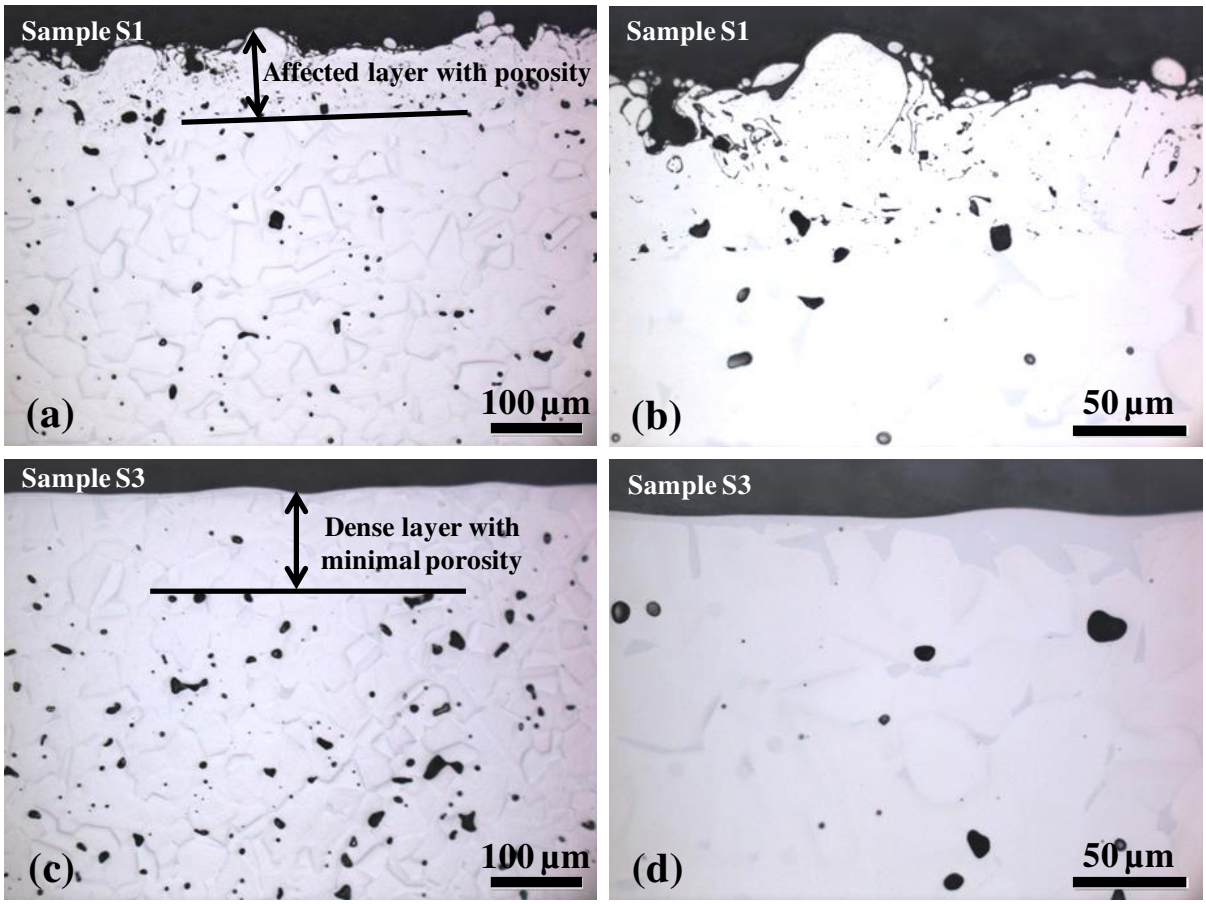

Fig. 20 Optical micrographs of un-etched cross-sections of LP specimens: (a) & (b) in air at E_d=20 J/cm^2; (c) & (d) in argon at E_d=9 J/cm^2.

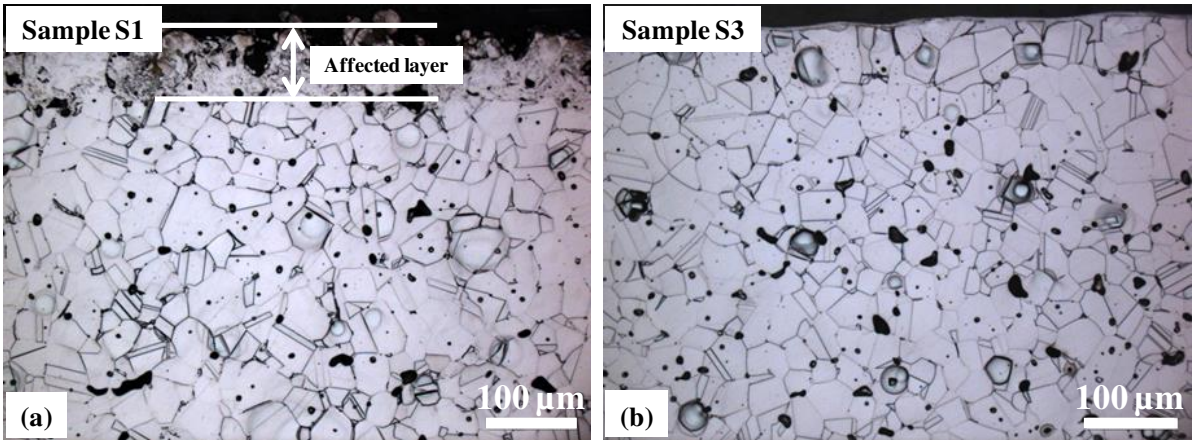

Fig. 21 Microstructure of laser polished specimens: (a) S1; (b) S3.

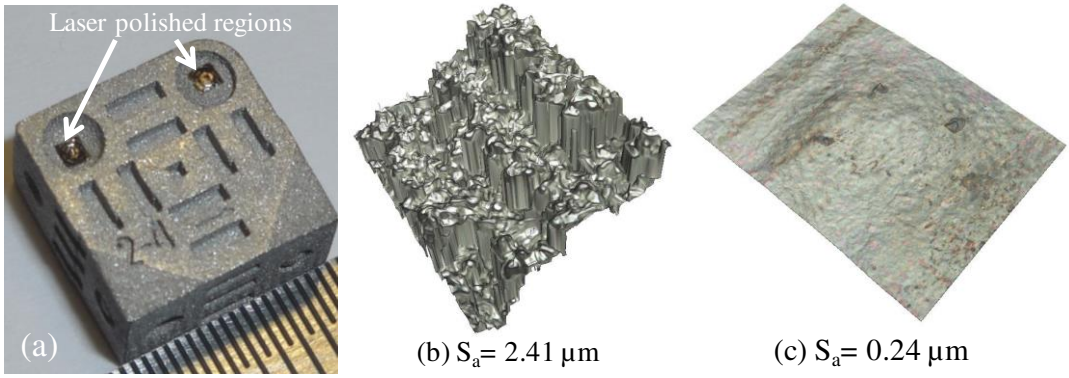

Fig. 22(a) LP regions on DM SS316L parts; (b) as-received DM surface; (c) LP surface, (area: 287×218 µm).

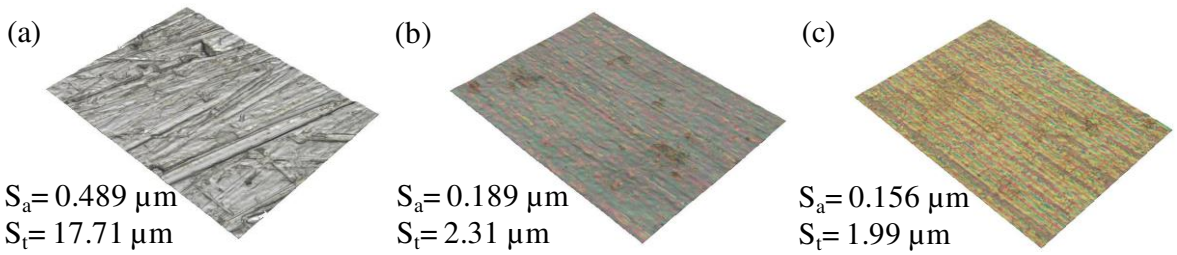

Fig. 23(a) Intermediately polished surface of aesthetic part, (b) and (c) laser polished surfaces, (area: 287×218 µm).

Table 1: Key publications on laser polishing of various engineered materials

References	**Year**	**Workpiece material**	**Laser type**	**Pulsed/ conti-nuous**	**Laser power (W)**	**Laser spot diameter (mm)**	**Energy density (J/cm^2)**	**Laser scan speed (mm/s)**	**Scan spacing/ step-over (mm)**
[5] Gu et al.	1997	CVD diamond films	Nd-YAG			0.1		0.1	0.05
[6] Pimenov et al.	1999	CVD diamond plates	Cu-vapour laser (λ=510 nm), ArF excimer laser (λ=193 nm)	Pulsed			Cu-vapour laser - 2.2, 6.5 Excimer laser - 98		
[7] Bol'shepaev and Katomin	1997	Fused silica	CO_2	CW	25-100				
[8] Wang et al.	2003	Silica slotted rods	CO_2	CW	5.8-40	0.2-1.0		5-10	0.05-0.8
[10] Hildebrand et al.	2011	Quartz glass	CO_2	CW	490-830			15-25	
[11] Heidrich et al.	2014	Glass	CO_2	CW	1500 max	0.45			
[12] Brinksmeier et al.	2004	X40Cr13 stainless steel moulds	Nd-YAG		50-100	0.2		1.33-8.33	
[13] Avilés et al.	2011	AISI 1045 carbon steel	Diode laser	CW	150.19-506.68	0.9 (top hat)	166-560	100.5	0.2

[15] Ukar et al.	2010	DIN 1.2379 (AISI D2) tool steel	Diode laser, CO_2 laser	CW	Diode - 250-1300 CO_2 - 800-1600	Diode - 2 CO_2 - 1.04		Diode - 23.33-40, CO_2 - 16.67-23.33	
[20] Guo et al.	2012	AISI O1 tool steel	Nd:YAG	Pulsed		1.26	10.03-80.24	1.67-8.33	
[21] Hafiz et al.	2012	AISI H13 tool steel	Nd:YAG	CW	300	1.0	3500	10	0.025, 0.05, 0.1, 0.2
[18] Pfefferkorn et al.	2014	AISI S7 tool steel	Fibre laser	Pulsed	5.5-80	0.03-0.197		100	0.0025-0.04
[22] Morrow et al.	2014	AISI S7 tool steel	Fibre laser	Pulsed	200 max	0.03-0.2	0.637-8.15		
[23] Wang et al.	2015	AISI S7 tool steel	Fibre laser	Pulsed	5.49	0.03		100	0.01
[19] Chang et al.	2016	SKD61 (AISI H13) tool steel	Yb-doped fibre laser	Pulsed	80-200			200-400	
[24] Vadali et al.	2012	SS316L stainless steel	Fibre laser	Pulsed	50 max	0.03		1500 max	
[25] Ukar et al.	2013	GGG70L cast iron	Fibre laser		100-250	0.1		100-300	
[26] Perry et al.	2009	Nickel	Nd:YAG	Pulsed	250 max	0.05, 0.11		1, 67	
[27] Hafiz et al.	2014	Inconel 718	MOPA ps laser	Pulsed	12	0.0314-0.0451	0.13-0.24	20	

[28] Perry et al.	2009	Ti-6Al-4V	Nd:YAG	Pulsed	250 max	0.05, 0.07		35, 40	0.025
[29] Vadali et al.	2012	Ti-6Al-4V	Nd:YAG, fibre lasers	Pulsed	250 max, 200 max			1500 max	
[31] Pfefferkorn et al.	2013	Ti-6Al-4V	Fibre laser	Pulsed	2.55, 3.38	0.0375, 0.0424		192, 224	
[33] Nüsser et al.	2013	Ti-6Al-4V	Nd:YAG	Pulsed	50	0.25		1000	0.03
[35] Giorleo et al.	2015	Titanium	$Nd:YVO_4$	Pulsed	2.55	0.06		5500	
[36] Remos-Grez and Bourell	2004	Selective laser sintered parts	CO_2	CW	225-565	0.4	116-850	101-850	
[37] Lamikiz et al.	2007	Selective laser sintered AISI 420 stainless steel (60%) infiltrated with bronze (40%)	CO_2	CW	600-1200	0.54-1.3	1385-16667	13.33-33.33	0.7-1.5
[2] Kruth et al.	2009	Selective laser melted (SLM) SS316L	Nd:YAG (λ=1064 nm)	CW	61-105	0.08-0.2		50-800	0.02
[38] Yasa et al.	2011	SLM SS316L parts	Diode-pumped Nd:YAG (λ=1064 nm)	CW	60-105	0.08-0.18		50-800	0.01-0.125

[41] Marimuthu et al.	2015	SLM Ti-6Al-4V components	Fibre laser (λ=1070-1090 nm)	CW	50-200	0.5		3.33-40	0.25
[1] Vaithilingam et al.	2016	SLM Ti-6Al-4V components	Fibre laser (λ=1070 nm)	Pulsed	200				0.1
[42] Rosa et al.	2015	Laser clad SS316L	Fibre laser		210	0.8	525	50	

Table 2: Nominal composition of Digital Metal® SS316L grade stainless steel [45]

Elements	Cr	Ni	Mn	Mo	S	C	Si	P	Cu	Fe
Wt%	16.5	10.4	1.36	2.09	0.007	0.025	0.58	0.02	0.1	Bal.

Table 3: Variable LP parameters and their corresponding levels

Process variables	**Levels**				
Fluence/Energy density (J/cm^2)	5		7		9
Pulse overlap factor along X (%)	82	85	88	91	95
Pulse overlap factor along Y (%)	82	85	88	91	95

Table 4: Analysis of variance for S_a

Source	**Degrees of freedom**	**Sum of squares**	**Mean squares**	**F-calculated**	**PCR**
E_d	2	1.77	0.88	46.24*	12.20
OP_x	4	7.23	1.81	94.54*	49.89
OP_y	4	1.34	0.34	17.59*	9.28
$E_d \times OP_x$	8	1.81	0.23	11.87*	12.53
$E_d \times OP_y$	8	0.51	0.06	3.34*	3.52
$OP_x \times OP_y$	16	1.21	0.08	3.96*	8.36
Error	32	0.61	0.02		4.22
Total	74	14.48			100
* Statistically significant at 95% confidence level					

Table 5: EDX spot analysis of LP and parent surfaces

Elements	Fe	Cr	Ni	O	C	Mo	Si
Spot 1 in Fig. 12(a)	66.8	18.2	4.8	6.3	2.9	0.5	0.3
Spot 2 in Fig. 12(a)	65.2	17.6	10.6	0.8	2.9	2.1	0.4

Table 6: Percentages of Fe, Cr and Ni oxides in the specimens LP in Ar and air

E_d (J/cm^2)	LP in argon				LP in air					
	Fe 2p % oxidised		Cr 2p % oxidised		Fe 2p % oxidised		Cr 2p % oxidised		Ni 2p % oxidised	
	Surface	After ion etching	Surface	After ion etching	Surface	After ion etching	Surface	After ion etching	Surface	After ion etching
20	94.85	60.00	100.00	80.29	100.00	100.00	100.00	100.00	100.00	66.63
19	92.04	54.67	100.00	65.38	100.00	100.00	100.00	100.00	100.00	63.32
18	91.98	54.37	95.98	63.10	100.00	99.05	100.00	100.00	100.00	58.83
16	90.52	54.03	95.03	62.30	100.00	98.96	100.00	100.00	100.00	58.60
13	68.38	53.81	84.14	52.66	100.00	97.30	100.00	100.00	100.00	57.40
9	67.48	51.89	74.45	50.88	100.00	96.24	100.00	100.00	100.00	55.24